

**STUDY OF THE MOTOR COGNITIVE  
INTERACTION DURING WALKING USING  
TRANSCRANIAL DOPPLER**

by

**Arthur Gatouillat**

B.S. in Electrical Engineering, INSA de Lyon, 2014

Submitted to the Graduate Faculty of  
the Swanson School of Engineering in partial fulfillment  
of the requirements for the degree of  
**Master of Science**

University of Pittsburgh

2015

UNIVERSITY OF PITTSBURGH  
SWANSON SCHOOL OF ENGINEERING

This thesis was presented

by

Arthur Gatouillat

It was defended on

June 1, 2015

and approved by

Ervin Sejdić, Ph. D., Assistant Professor

Department of Electrical and Computer Engineering

Zhi-Hong Mao, Ph. D., Associate Professor

Department of Electrical and Computer Engineering

Murat Akcakaya, Ph. D., Assistant Professor

Department of Electrical and Computer Engineering

Thesis Advisor: Ervin Sejdić, Ph. D., Assistant Professor

Department of Electrical and Computer Engineering

# STUDY OF THE MOTOR COGNITIVE INTERACTION DURING WALKING USING TRANSCRANIAL DOPPLER

Arthur Gatouillat, M.S.

University of Pittsburgh, 2015

Gait is a complex process involving both cognitive and sensory ability and is strongly impacted by the environment. In this thesis, we propose the study of the impact on cognitive task during gait on the cerebral blood flow velocity through a dual task methodology. Both cerebral blood flow velocity and gait characteristics of eleven participants with no history of brain or gait conditions were recorded using transcranial Doppler on mid-cerebral artery and a treadmill. The cognitive task was induced by a backward counting starting from 10,000 with decrement of 7. Central blood flow velocity raw and envelope features were extracted in both time, frequency and time-scale domain along with information-theoretic metrics were extracted, and statistical significances. A similar feature extraction was performed on the stride interval signal. Statistical differences between the cognitive and baseline trials, between the left and right mid-cerebral arteries signals and the impact of the anthropometric variables were studied using linear mixed models. No statistical differences were found between the left and right mid-cerebral arteries flows or the baseline and cognitive state gait features, while statistical differences for specific features were measured between cognitive and baseline states. These statistical differences found between the baseline and cognitive states show that cognitive process has an impact on the cerebral activity during walking. The state was found to have an impact on the correlation between the gait and blood flow features.

**Keywords:** transcranial Doppler, gait accelerometry, cerebral blood flow velocity, walking, signal features.

## TABLE OF CONTENTS

<b>PREFACE</b> . . . . .	viii
<b>1.0 INTRODUCTION</b> . . . . .	1
1.1 HUMAN GAIT ANALYSIS . . . . .	1
1.1.1 The Human Walk: a Quick Overview . . . . .	1
1.1.2 Moto-Cognitive Interferences . . . . .	3
1.2 FUNCTIONAL BRAIN IMAGING . . . . .	4
1.2.1 Brain Imaging Techniques and Transcranial Doppler . . . . .	4
1.2.2 Comparison of Brain Imaging Techniques . . . . .	7
1.3 RESEARCH OBJECTIVE . . . . .	8
<b>2.0 BACKGROUND</b> . . . . .	10
2.1 STUDYING HUMAN GAIT . . . . .	10
2.1.1 Usually Defined Human Gait Characteristics . . . . .	10
2.1.2 Collecting Gait Features: an Overview . . . . .	10
2.1.2.1 Using Computer Vision to Access Gait . . . . .	10
2.1.2.2 The Use of Accelerometers to Investigate Walking . . . . .	12
2.1.2.3 Employing Pressure Sensitive Surface to Study Gait . . . . .	12
2.2 THE ARTERIES OF THE BRAIN . . . . .	14
2.2.1 The Circle of Willis . . . . .	14
2.2.2 Insonating the Middle Cerebral Arteries . . . . .	16
2.3 MEASUREMENT OF THE CEREBRAL BLOOD FLOW VELOCITY WITH TRANSCRANIAL DOPPLER . . . . .	17
2.3.1 Modeling the Ideal Cerebral Blood Flow . . . . .	17

2.3.2	The Doppler Effect . . . . .	18
2.3.2.1	Introduction to the Doppler Effect . . . . .	18
2.3.2.2	Blood Flow Velocity Estimation . . . . .	20
<b>3.0</b>	<b>METHODOLOGY . . . . .</b>	<b>24</b>
3.1	DATA ACQUISITION . . . . .	24
3.2	ANALYSIS OF STRIDE INTERVAL TIME SERIES . . . . .	25
3.3	ANALYSIS OF MCA SIGNALS . . . . .	27
3.3.1	Statistical features . . . . .	27
3.3.2	Information-theoretic features . . . . .	28
3.3.3	Frequency features . . . . .	31
3.3.4	Time-frequency features . . . . .	32
3.4	STATISTICAL TEST . . . . .	36
<b>4.0</b>	<b>RESULTS . . . . .</b>	<b>37</b>
4.1	STRIDE INTERVAL FEATURES . . . . .	37
4.2	MCA SIGNAL FEATURES . . . . .	38
4.2.1	Time features . . . . .	38
4.2.2	Information-theoretic features . . . . .	38
4.2.3	Frequency features . . . . .	39
4.2.4	Time-frequency features . . . . .	39
4.2.5	Correlation between left and right MCA blood flow . . . . .	40
4.3	CORRELATION BETWEEN GAIT AND MCA FEATURES . . . . .	41
4.4	IMPACT OF ANTHROPOMETRIC VARIABLES ON FEATURES . . . . .	42
<b>5.0</b>	<b>DISCUSSION AND LIMITATIONS . . . . .</b>	<b>44</b>
5.1	DISCUSSION . . . . .	44
5.2	LIMITATIONS OF THE STUDY . . . . .	45
<b>6.0</b>	<b>CONCLUSIONS AND FUTURE WORK . . . . .</b>	<b>46</b>
6.1	CONCLUSIONS . . . . .	46
6.2	FUTURE WORK . . . . .	46
	<b>BIBLIOGRAPHY . . . . .</b>	<b>48</b>

## LIST OF TABLES

1.1	Comparison of functional brain imaging techniques . . . . .	7
2.1	Flow characteristics of the cerebral arteries . . . . .	15
4.1	Stride interval features . . . . .	37
4.2	Time features from raw and envelope CBFV signals . . . . .	38
4.3	Information-theoretic features from raw and envelope CBFV signals . . . . .	39
4.4	Frequency features from raw and envelope CBFV signals . . . . .	40
4.5	Wavelet entropy values for raw and envelope CBFV signals . . . . .	40

## LIST OF FIGURES

1.1	Illustration of the human gait cycle . . . . .	3
1.2	Timeline of major advances of the functional brain imaging field using fMRI and PET . . . . .	6
2.1	Commonly used gait performance features . . . . .	11
2.2	Illustration of a silhouette extraction algorithm . . . . .	12
2.3	Acceleration time series of the right ankle during walking, vertical direction . . . . .	13
2.4	Average foot pressure and maximum foot pressure of a selected subject in our study . . . . .	14
2.5	Circle of Willis . . . . .	15
2.6	Experimental set-up to collect left and right MCA blood flow signals . . . . .	16
2.7	Ideal parabolic velocity distribution of the cerebral blood flow . . . . .	18
2.8	Illustration of the Doppler effect . . . . .	20
2.9	Illustration of the Doppler effect and insonation angle in the context of blood flow velocity measurement . . . . .	21
2.10	Illustration of the quadrature demodulation technique . . . . .	22
2.11	Illustration of the Hilbert transform technique . . . . .	22
3.1	TCD System and treadmill used for the data collection . . . . .	25
3.2	Illustration of the 10 levels discrete wavelet transform algorithm. . . . .	34
3.3	Plot of the Meyer mother wavelet . . . . .	35
4.1	The 10 level wavelet decomposition of raw signals . . . . .	41
4.2	The 10 level wavelet decomposition of envelope signals . . . . .	41
4.3	Correlation and adjusted correlation in the baseline and cognitive states. . . . .	43

## PREFACE

I would like to thank INSA de Lyon and Dr. Mahmoud El Nokali for giving me the opportunity to study at the University of Pittsburgh Swanson School of Engineering. I would like to express my gratitude to my advisor, Dr. Ervin Sejdić, for his guidance and his precious advices. I express my gratitude to Dr. Jessie VanSwearingen and Dr. Subashan Perera for their help with the interpretation of my results and to conduct the statistical analysis. I would also like to thank my colleagues, my family, my friends and Felipe for their support during this year abroad.

## 1.0 INTRODUCTION

### 1.1 HUMAN GAIT ANALYSIS

#### 1.1.1 The Human Walk: a Quick Overview

Walking is a complex sensory-cognitive interaction which has various demands depending on the environment [1, 2, 3], and it was considered as a topic of interest as early as the Greek antiquity with Aristotle (384 – 322 BCE), who first commented, without the support of any experimental argument, the human gait [4].

It was however much later, during the Renaissance, that this field was explored further using the breakthrough achieved at that time: in physics, with the contribution of Newton that allowed who conceptualized forces; in mathematics, with the improvement of a wide variety of geometrical concepts; and eventually in anatomy. The advances in photography realized 20th century allowed to improve the capture of the position of the human body during walking [4].

Nowadays, several techniques are widely used to access human gait: the most commonly used method is to employ video combined with computer vision algorithms to extract gait features [5, 6], accelerometers [7, 8, 9, 10], or pressure mapping surfaces [11, 12]. This modern techniques allowed to achieve a complete description of the gait.

Gait characteristics deterioration can be caused by a wide amount of causes: neurodegenerative disorders such as Parkinson’s or Huntington’s disease [13], lower-limb joint disease [14, 15] or ageing [16, 17]. Because of the strong impact of gait on the quality of life of the patients [18], developing diagnostics tools to assist the physicians with the medical management of patients presenting a walking disorder [19] is crucial.

Several research directions about gait and unrelated to the medical field. One of the recent areas of study is the biometric identification using gait features [20]. The research in this area began with the investigation of the ability for humans to identify a subject by its gait [21, 22]. Later, development of computer vision allowed performing feature extraction and recognition can be realized [20]. The features can either be holistic or model parameter identification, yielding in encouraging results in terms of subject recognition with potential practical implementation [20].

Another challenging field where human gait analysis is of interest is in the improvement of the design of biped robots [20]. The main idea is to identify a human gait model and its parameters to allow a stable walk in a static environment, or more ideally on different kind of surfaces [20, 23]. Several designs of biped robots mimicking human gait have been successful [24, 25].

Human gait is initiated with a shift of the center of mass of the body outside the base of support. Then, a series of steps is initiated, where legs are moved forwardly alternatively and where the center of mass is always located outside of the base of support. Because of the periodic nature of this motion, a stride cycle can be described. The cycle is divided into two phases: the stance phase and the swing phase. The right leg stance phase begins when the right heel hits the ground. The right leg supports the body during the entire stance phase, and this phase ends when the right toes leave the ground. The right leg is then swung while the left leg supports the body. This is called the right swing phase. Please note that the right and left phases are inverted and overlapping. The overlapping periods are called double support periods [26]. This cycle is the equivalent of two steps and its components are given in Figure 1.1.

However, one must realize that walking is not only the result of a simple alternative leg swinging, and that the processing of several sources of information (such as vision or touch to maintain equilibrium) is necessary to achieve movement [28].

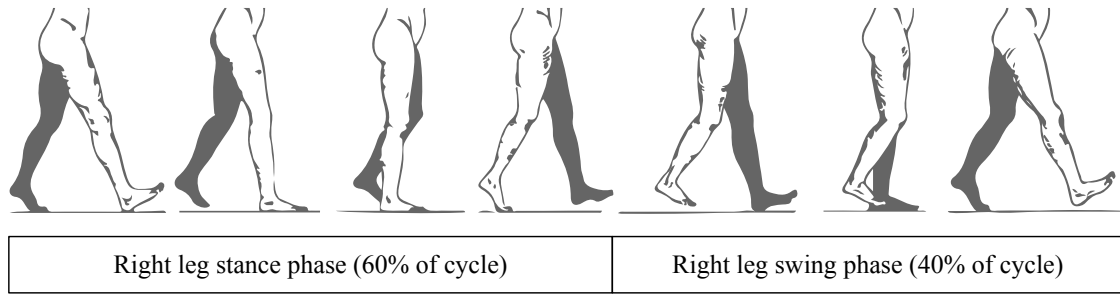


Figure 1.1: Illustration of the human gait cycle. Adapted from Schafer (1987) [27].

### 1.1.2 Moto-Cognitive Interferences

Initially, cognition and motor control of gait have been believed to be two completely autonomous processes, with walking regarded as an automatic motor function, independent of any cognitive tasks [29, 30]. However, recent research shows that a cognitive load has an effect on gait [31, 32, 33], and that gait measures and executive function are correlated [29].

The executive functions indicate cognitive processes that controls the information produced by cortical sensory systems located in the anterior and posterior brain regions to generate behavior [34]. These functions make use of both intellectual and behavioral factors that are crucial to achieve goal-directed action and for the regulation of attentional resources. Both of these components are fundamental to achieve independent activity of daily living. The executive functions can be divided into four components: volition (which is the capacity to formulate an intention), planning, purposive action and effective performance, and an impairment of each of this component has an effect on gait [29, 35].

Ordinarily, executives functions have been associated with the frontal lobes of the brain, and several regions of this lobe (dorsolateral prefrontal cortex and cingulate cortex) have been found to be correlated to the cognitive requirements of these functions [29, 35]. However, the imaging studies performed in order to localize the brain regions origin from where the executive functions originate suggest that these functions are based on a network between the anterior and posterior brain areas [36, 29]. Similar conclusion where also drawn thanks to the study of the executive functions performance of patients presenting localized brain damages [37].

In fact among persons with pathological conditions, the dual-task methodology was mainly used to observe the effect of concurrent stimuli while checking the gait state [38]. This technique may underline a cognitive-motor interference that indicates a conflict between concurrent tasks (i.e. a motor and a cognitive challenges), as there may be a deterioration of one or both of the tasks [38, 39].

In general, a dual task (i.e. a cognitive stimulus/walking) causes concurrent demands for attention/cognitive resources. Hence, it generates a cognitive-motor interference that implies tripping, falling, physical instability and/or a decline in the gait performance [29, 2, 40]. These falls occur mainly for elderly subjects and have a strong impact on the health of elderly subjects [31]. These events also have an impact on the health costs [41], and the risk of falling is associated with gait disruptions [42]. Prior studies have illustrated that individuals with neurodegenerative disorders, those recovering from stroke or elderly adults, are more prone to the effects of cognitive load on gait [32, 38, 43]. On the opposite, just a few investigations have investigated the cerebral repercussions of a dual-task in the case of able-bodied young participants [44]. Moreover, there has been limited research on the effects of cognitive load on the cerebrovascular system during gait.

Because of the elderly population life quality and health concern, there is a growing interest in clarifying the correlation between motor control and cognition. Brain imaging methods have revealed activation of various cerebral regions associated with higher cognitive functions during walking (i.e. the dorsolateral prefrontal cortex and anterior cingulate cortex [45, 46, 47, 48]).

## 1.2 FUNCTIONAL BRAIN IMAGING

### 1.2.1 Brain Imaging Techniques and Transcranial Doppler

Estimating the response of the brain to a wide variety of stimuli or when various task are realized is a crucial step in the understanding of how it operates, thus became essential in neuroscience. Presently, several functional imaging methods are available and widely used:

functional magnetic resonance imaging (fMRI), magnetic resonance spectroscopy (MRS), computed tomography (CT), positron emission tomography (PET) and single positron emission computed tomography (SPECT) [49]. A timeline of the major advances in the functional imaging field is given in Figure 1.2. All of these techniques localize and record regional changes in the brain activity, such as regional brain circulation and metabolism [50]. These records are then used to link anatomical changes to neural activation. An oversimplifying reason of the alteration of the cerebral blood-flow during cognition is that specific brain region require an increased amount of glucose and oxygen to satisfy the active zone energy need [51], particularly, this changes in the brain irrigation topology has been shown to exhibit some changes during the processing of mathematical tasks [52]. The MRS technique also uses magnetic information, but where the fMRI uses this information to form images, the MRS uses it to gather concentration of a wide variety of brain metabolites [53].

More specifically, the fMRI tracks the hemodynamic activity using a method called blood oxygenation level-dependent (BOLD) [54]. A simplified way to understand this method is that the oxygenation of the blood flow in the brain is measured based of the difference of magnetic susceptibility between oxygenated and desoxygenated blood flow [55]. Because of this difference in the magnetic property of the blood depending on its oxygenation/desoxygenation rate, it will appear with an altered intensity on the MRI images. This method is widely used in the study of cognitive processes [56], and is appreciated because of its non-invasive characteristics [57].

The CT scan uses multiple X-Ray images taken from different angles and combines them into a reconstructed 2D “body-slices” representation or a 3D representation [58]. This method, coupled with advanced image processing techniques, can be used to monitor the brain perfusion [59]. Even though it is minimally invasive, the ionizing nature of X-rays used by this technique and the associated cancer risks makes its repeated use dangerous for the patients [60, 61].

The PET scan monitors brain activity using the detection of the gamma ray emitted by a radionuclide. The radionuclide has to be  $\beta^+$  radioactive, i.e. emitting protons while decaying [62]. This radionuclide, also called tracer, is embedded in the body using metabolically active molecules [62]. The PET scanner then detects the tracers’ regional radioactivity and through

signal processing techniques, reconstructs a 3D static or time varying representation of the brain [62]. The SPECT scan works similarly. These techniques, because of the necessity of the injection of a radio-tracer in the body, can not be considered as minimally invasive.

The blood flow changes occurring during cognition can also be monitored using transcranial Doppler. Aaslid et al. introduced TCD as a non-invasive method of real-time measurement through the skull of the main cerebral arteries blood flow velocity and its variation [63]. Since the perfusion area and the diameter of the cerebral arteries do not change during a cognitive process [64, 65, 66], the blood flow alterations are due to changes in the brain metabolism, and because of its close relationship to the blood flow, the velocity measurement can be used to access a mental task characteristics. The effect of a wide range of different tasks such as visual stimuli [67], auditory stimuli [68] or memory tasks [69] on TCD signals has been widely studied.

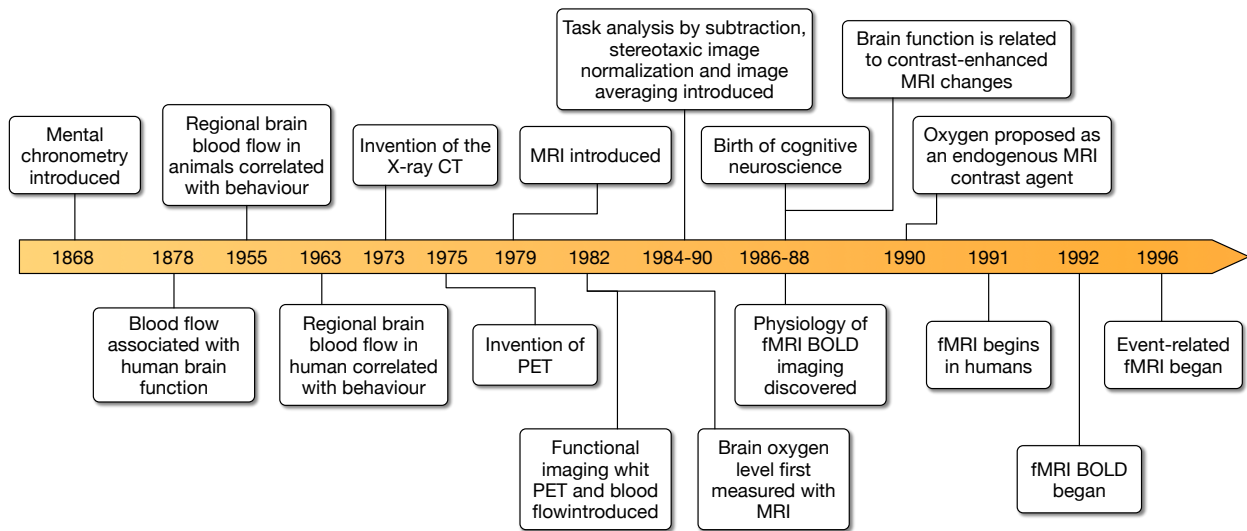


Figure 1.2: Time line of major advances of the functional brain imaging field using fMRI and PET. Adapted from Raichle (2009) [70].

## 1.2.2 Comparison of Brain Imaging Techniques

This research is focused on accessing the effect of a cognitive load during walking on the cerebral blood flow. All the procedures described herein above can retrieve information on the cerebral blood flow, and comparing the different available functional imaging devices will allow us to choose the more appropriate technique for our study.

The study of the advantages and drawbacks of each of the functional brain imaging method is given in Table 1.1. Of all the functional brain imaging presented herein above, all of them have been used to model the brain activity while walking. However, because of the lack of portability of these devices and the fact that they require the subject to lie down during the acquisition, the gait is usually modeled as a series of feet tapping in the fMRI case [71, 72] and it is studied by the injection of a radio-tracer, the walking sequence, and a scan for the PET/SPECT case [73, 74]. These devices, because of their lack of portability and the strong constraints associated with their use, are not optimal to perform a real time study of the brain during walking. Even though these techniques do present a good spacial resolution, these methods features a poor temporal resolution.

Table 1.1: Comparison of functional brain imaging techniques. Adapted from Min (2010) and Khalil (2011) [75, 76].

Type	Advantage	Disadvantage	Cost
fMRI	<ul style="list-style-type: none"> <li>• Excellent spacial resolution</li> <li>• Entire brain acquisition</li> <li>• Non invasive</li> </ul>	<ul style="list-style-type: none"> <li>• Poor temporal resolution</li> <li>• Incompatibility with ferro-magnetic materials</li> <li>• Poor mobility</li> <li>• High maintenance costs</li> </ul>	High ( $\approx$ Few millions \$)
PET	<ul style="list-style-type: none"> <li>• High sensitivity</li> <li>• Good spatial resolution</li> </ul>	<ul style="list-style-type: none"> <li>• Partially invasive (injection of a radio-tracer needed)</li> <li>• Poor mobility</li> <li>• Short acquisition window because of the short half life of radio-tracers.</li> </ul>	High ( $\approx$ Few millions \$)
SPECT	<ul style="list-style-type: none"> <li>• High sensitivity</li> <li>• Use of long half life radio-tracers possible</li> </ul>	<ul style="list-style-type: none"> <li>• Partially invasive (injection of a radio-tracer needed)</li> <li>• Poor mobility</li> <li>• Low spacial resolution</li> </ul>	High ( $\approx$ Few hundreds of thousands \$)
fTCD	<ul style="list-style-type: none"> <li>• Good portability</li> <li>• Good temporal resolution</li> <li>• Non invasive</li> </ul>	<ul style="list-style-type: none"> <li>• Low spacial resolution</li> <li>• Difficulties in finding the correct insonation path</li> <li>• Constrained to target large vessels</li> </ul>	Low ( $\approx$ Few thousands)

However, the TCD, because of its portability, can be used to perform a functional study of the brain during walking, provided that the subject is asked to walk on a treadmill. Furthermore, this method was highlighted by numerous publications for its excellent temporal resolution [77], non-invasive and minimally stressful characteristics [78, 79].

Another strong argument in favor of the transcranial Doppler is its cost: high-spatial temporal resolution techniques feature very high purchasing and maintenance costs [80, 81]. The cost of these procedures originates from different sources: installation, material, radio-tracers, personnel formation [80, 81]. Moreover, the operating of such imaging devices requires appropriately trained technical personnel. Conversely, the transcranial Doppler can be operated following a very short timing. Additionally, its low purchasing costs and absence of regular maintenance makes it an extremely cost-efficient method compared to the fMRI or PET/SPECT scans.

### 1.3 RESEARCH OBJECTIVE

The current study was focused on studying the associations between the cerebrovascular system and gait and understanding the repercussions of cognitive load during walking on this system. Specially, we examined CBFV signals in MCA. We examined both raw signals and the envelope signals, which are maximum peak velocity outcomes.

Since it has been proven that CBFV modifications and neural activity can be correlated [82, 83, 84, 85, 86, 86], we used transcranial Doppler recordings to monitor hemodynamic activities of the main cerebral arteries [87] to study a motor-cognition interaction. Readings were taken with ultrasonic transducers, placed bilaterally in the transtemporal window of the skull of one participant, which allowed the monitoring of the left and right side of the circle of Willis' cerebral arteries [88, 89, 90, 91]. Most studies focused on activities of the middle cerebral artery (MCA) given that the MCA carries more than 80% of blood to the brain [92]. Moreover, previous papers highlighted brain perfusion changes during neural cognitive challenges [93, 51, 94]. Concerning physical performance, global cerebral blood flow (CBF) appears to be increased, unchanged or decreased during stimuli [95, 96, 97]. Nevertheless, a regional increase of CBF was noticed during physical exercise [98].

These signals were inspected along with gait-related features, and our major findings include a comprehensive assessment of both the raw and envelope signals of the TCD in the time, frequency, information-theoretic and time-frequency domain, along with the inspection of the correlation between TCD features and gait features. Our major contributions are the statistical differences found in the central blood flow velocity signals between the baseline and cognitive states during walking. The feature extraction process is described in Chapter 3, while the results are given and discussed in Chapters 4 and 5 respectively.

## 2.0 BACKGROUND

### 2.1 STUDYING HUMAN GAIT

#### 2.1.1 Usually Defined Human Gait Characteristics

The literature about human walking and dual-task methodology considered an important amount of features aiming to accurately represent the gait performance. These metrics, along with their use frequency, are summarized in Figure 2.1.

Even though the walking speed is the most commonly used feature, our experimental setup prevents us to use it because the subjects are required to walk on a treadmill at a fixed speed. Our final choice of features was the mean stride time, coefficient of variation (ratio of the stride time standard deviation and the mean).

Moreover, it has been shown that the stride interval time series presents  $1/f^\beta$  noise properties [99, 100, 101]. The purpose of the fractal analysis is to compute a metric accurately representing the time process parameters and possible long term correlation [102, 99, 103]. Even though several metrics characterizing fractal processes have been proposed, we chose to compute the  $\beta$  coefficient because of its relation to numerous other fractal parameters [102]. Because of the significant amount of information carried by this parameter, we chose to evaluate it along with the other features described here-in above.

#### 2.1.2 Collecting Gait Features: an Overview

**2.1.2.1 Using Computer Vision to Access Gait** One of the widely used technique available to study gait characteristics is the use of video and appropriate algorithm to extract the features of interest. One of the commonly used process is based on silhouette extraction

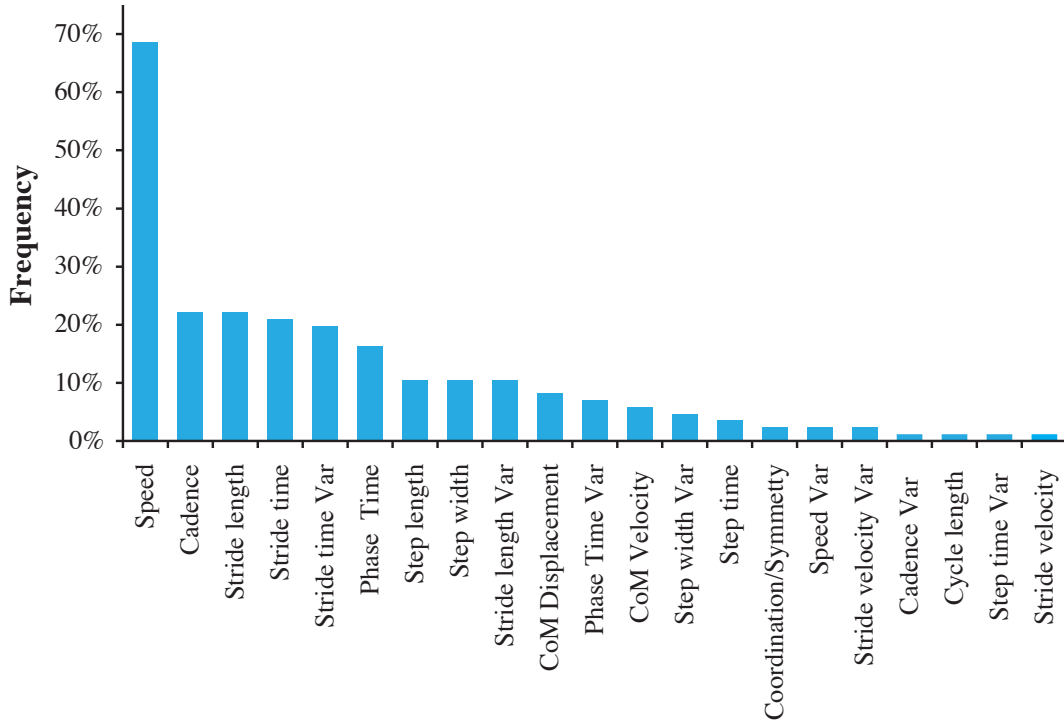


Figure 2.1: Commonly used gait performance features. Adapted from Al-Yahya (2011) [2].

from the video. The silhouette of the walker, defined by the region of pixels the subject occupies, is extracted either using simple background subtraction and thresholding (thus requiring a knowledge of the background without the subject) [104] or more sophisticated algorithms, based on the statistical analysis of the pixels and advances detection and estimation techniques [6] or the modeling of the background [105]. An example of the feature extraction algorithm is given in Figure 2.2.

Then, features such as the gait period can be extracted. To do so, several approaches have been considered: the simplest approach is to count the amount of pixels in the lower half of the silhouette (i.e. the silhouette representation of the legs), assume that this number will be maximized when the legs will be the farthest apart and eventually consider that the time between two of these events can be considered as the gait period [6]; or with the use of stance phases frame identification [104]. Other features such as silhouette contour and centroid have been used [105] for identification intents. Furthermore, methods based

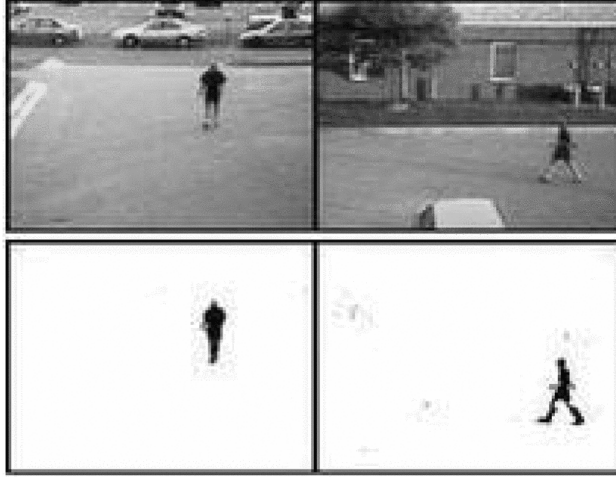


Figure 2.2: Illustration of a silhouette extraction algorithm. Adapted from [104].

on motion tracking of the limbs during gait have also been proposed for both medical and identification purposes [106, 107].

Through this quick overview, we verified that it is possible to extract our chosen features, i.e. the stride interval time series, using video associated with computer vision algorithms.

**2.1.2.2 The Use of Accelerometers to Investigate Walking** Accelerometers can also be used to access gait parameters [7, 8, 9, 10]. The idea is to attach accelerometers to parts of the subject's body (the commonest location being trunk [7] and ankles [9]), and perform an analysis on the accelerometer time series to infer the gait characteristics. As displayed on Figure 2.3, it is possible to extract our feature of interest, the stride interval time series using a technique as simple as the attachment of an accelerometer to a limb of a subject. Please however notice that the placement of the accelerometer has to be determined carefully to obtain exploitable signals.

**2.1.2.3 Employing Pressure Sensitive Surface to Study Gait** Another method investigated by researchers is the use of pressure sensitive surfaces to extract gait characteristics [11, 12]. These materials allow retrieving a mapping of the pressure applied on them. Used in

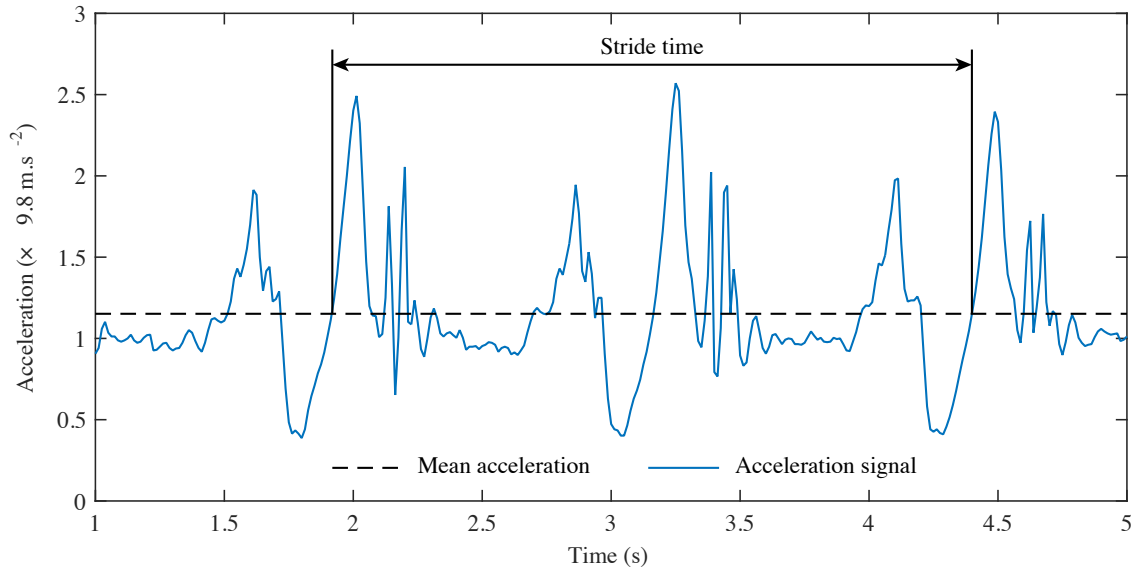


Figure 2.3: Acceleration time series of the right ankle during walking, vertical direction. Adapted from Ailisto (2005) [108].

the gait study context, the aim is to capture the pressure applied by the foot on the surface. These surface are composed of an array of resistive or capacitive pressure sensors. If the resistive technology is used, each cell presents a resistivity that changes as a function of the pressure applied on the material [109]. Then, the cells are interfaced using a voltage divider and the voltage-pressure relationship can be obtained trough accurate calibration. If the capacitive method is chosen, the output of the sensor will be a pressure varying capacity. Even though the interfacing of such sensors is often more difficult than their resistive counterparts, they usually feature an improved sensitivity [110].

In our cases, a treadmill equipped with 5,376 capacitive cells was available, so we chose this method to retrieve stride interval time series and perform the gait performance analysis. An example of the foot pressure mapping acquired by the treadmill is given in Figure 2.4.

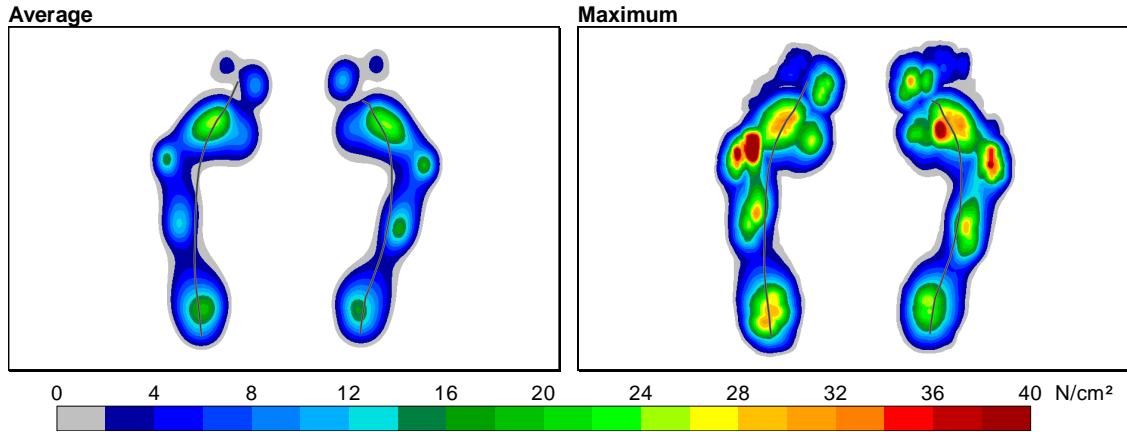


Figure 2.4: Average foot pressure and maximum foot pressure of a selected subject in our study.

## 2.2 THE ARTERIES OF THE BRAIN

### 2.2.1 The Circle of Willis

The transcranial Doppler is traditionally used to measure the blood flow velocity in the major cerebral arteries [91, 89, 111]. The transducers are placed on skull regions where the bone thickness is the thinnest. Three anatomical windows are usually considered: the transtemporal window, through which the mid-cerebral (MCA), anterior (ACA) and posterior (PCA) cerebral arteries; the transforaminal window, to access the blood flow of the vertebral (VA) and basilar (BA) arteries; and eventually the transorbital window, that allows gathering information on the ophthalmic (OA) and internal arteries. These arteries form the circle of Willis, displayed on Figure 2.5.

Once a flow is captured by the TCD, one can identify the artery where the flow resides by considering the set of characteristics used presented in Table 2.1. The ACA, MCA and PCA are the most insonated arteries, because each of these arteries supply blood to different brain regions, and because the blood flow in these arteries can characterize the neural activities in the irrigated regions [113, 114, 115].

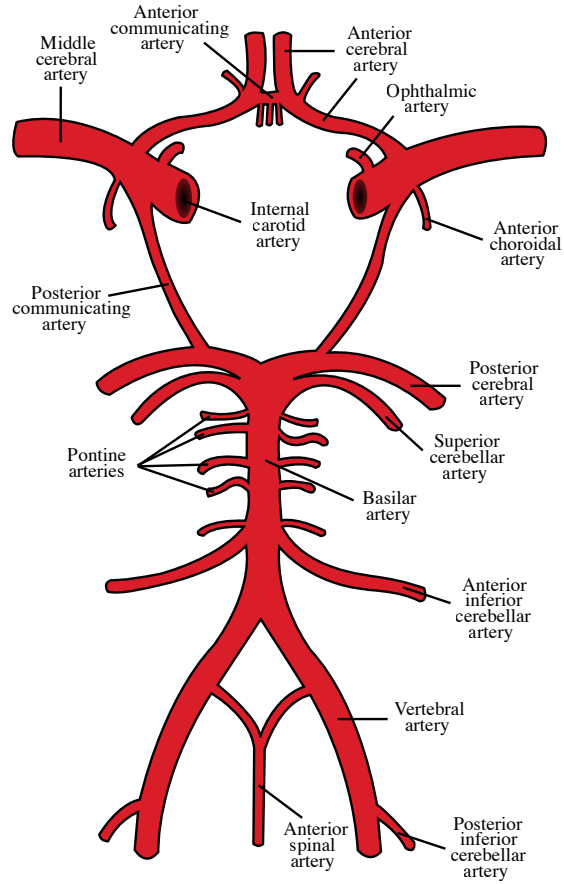


Figure 2.5: Circle of Willis. Adapted from Gray (1918) [112].

Table 2.1: Flow characteristics of the cerebral arteries. Adapted from White (2006) [91].

Artery	Window	Transducer orientation	Depth (mm)	Flow direction	Velocity (cm/s)
OA	Orbital	Slightly medial	40 – 50	Toward	16 – 26
MCA	Temporal	En face	35 – 60	Toward	46 – 86
ACA	Temporal	Anteriorly	60 – 75	Away	41 – 76
PCA	Temporal	Posteriorly	60 – 75	Toward	33 – 64
VA	Foraminal	Superiorly and obliquely	45 – 75	Away	27 – 55
BA	Foraminal	Superiorly	70 – 120	Away	30 – 57

### 2.2.2 Insonating the Middle Cerebral Arteries

In this thesis, we insonated the MCA because of its good ability to track a cognitive activity [116, 83, 82]. Additionally, this artery is easier to target with the Doppler probe. Two ultrasonic probes were placed on the transtemporal window of the patients, and they were moved until a good flow signal was found. When the optimal position was established, both the probes were fixed. An illustration of the experimental set-up is given in Figure 2.6.

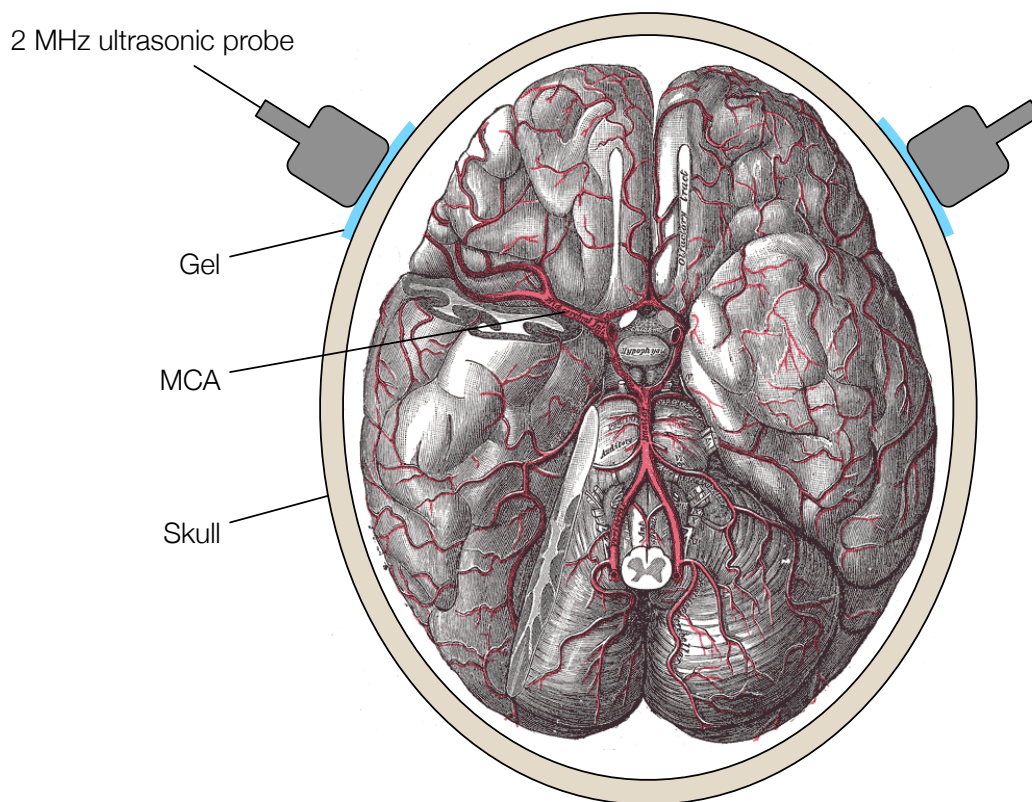


Figure 2.6: Experimental set-up to collect left and right MCA blood flow signals. Adapted from Gray (1918) [112].

## 2.3 MEASUREMENT OF THE CEREBRAL BLOOD FLOW VELOCITY WITH TRANSCRANIAL DOPPLER

### 2.3.1 Modeling the Ideal Cerebral Blood Flow

The TCD assumes that the blood flow velocity can be modeled as the laminar circulation of a fluid in a circular pipe. Under the assumption that the external forces can be neglected, that the flow is laminar, that the viscosity  $\eta$  does not depend on the velocity, that the diameter of the circle described by the pipe is constant, denoted as  $R_0$ , and eventually that the liquid is not compressible [51].

If these hypotheses are satisfied, the local velocity of the blood, denoted as  $v(r)$ , can be expressed as [51]:

$$v(r) = \frac{R_0^2 - r^2}{4\eta} \times \frac{p_1 - p_2}{\ell} \quad (2.1)$$

where  $p_1$  and  $p_2$  are pressure in the pipes separated with the distance  $\ell$ , and  $r$  the radius of the circles described by the sections of the pipe.

This equation describes a parabolic behavior and the velocity distribution is illustrated in Figure 2.7. The maximum blood flow velocity is located at the centre of the pipe ( $r = 0$ ), and it can be easily computed:

$$v_{\max} \triangleq v(r)|_{r=0} = \frac{R_0^2}{4\eta} \times \frac{p_1 - p_2}{\ell} \quad (2.2)$$

and  $v_{\max}$  is called the envelope signal [51].

One can also compute the mean velocity of the blood by averaging over the area described by the section of the pipe, and this velocity can be expressed as [51]:

$$v_{\text{mean}} = A^{-1} \iint_A v(r) \, dA = \frac{1}{2} \frac{p_1 - p_2}{4\eta\ell} R_0^2 = \frac{1}{2} v_{\max} \quad (2.3)$$

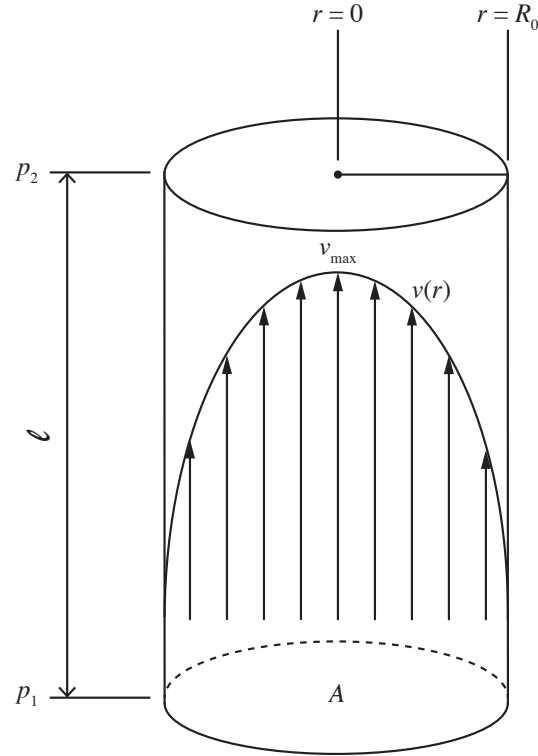


Figure 2.7: Ideal parabolic velocity distribution of the cerebral blood flow. Adapted from Deppe (2004) [51].

## 2.3.2 The Doppler Effect

**2.3.2.1 Introduction to the Doppler Effect** The Doppler effect was introduced by Christian Doppler in 1842. In a pulsed ultrasound Doppler, a frequency shift between the incident and reflected wave when the reflecting object is moving can be observed [111]. In the case of blood flow measurement, the reflector is composed of the erythrocytes composing the moving blood.

A simple illustrative example of the Doppler shift is given in Figure 2.8. In this example, the receiver, illustrated with a filled black circle, is moving at speed  $v$  with respect to the fixed transmitter. The emitted wave has a wavelength  $\lambda_0 = c/f_{\text{em}}$ . The lower part of the figures displays the state of the system at time  $T + 1$ , thus after one unit of time has passed.

Since the wavelength is constant, we can write [111]:

$$\lambda_0 = \frac{c}{f_{\text{em}}} = \frac{c+v}{f_1} \quad (2.4)$$

However, in the blood flow measurement case, both the transmitter and receiver are both gathered in the same device (called transceiver or Doppler probe), and the emitted wave is reflected by a moving object, as illustrated in Figure 2.9. During the measurement of the central blood flow velocity, the transceiver is placed with an angle  $\phi$  with regard to the blood flow direction, as displayed on Figure 2.9. The speed of one erythrocyte, denoted as  $v$ , can be computed using [51]:

$$v = \frac{c}{2 \cos \phi} \frac{\Delta f}{f_{\text{em}}} \quad (2.5)$$

where  $\Delta f$  is the frequency shift between the incident and reflected wave,  $f_{\text{em}}$  is the frequency of the emitted sound wave,  $\phi$  is the insonation angle and  $c$  is the velocity of the ultrasonic wave.

Please note that the insonation angle is usually unknown, but that transcranial color coded Doppler allows the angle-correction of the measure of the central blood flow velocity because of the acquisition of both anatomical and hemodynamic information [117].

The equation (2.5) only holds for one blood cell. Since the blood flow comprises many independent erythrocytes moving at different speed, the received signal is the sum of the contribution of each cell and can be written as [51]:

$$s_{\text{rec}} = s_{\text{em}}(f_{\text{em}}) + \sum_i a_i \sin(2\pi f_i t + \varphi_i) \quad (2.6)$$

where  $s_{\text{em}}(f_{\text{em}})$  accounts for the reflection on the static tissue,  $a_i$  represents the contribution of each moving component and  $\varphi_i$  is the phase shift associated with each of these components.

One can easily notice the similarities between the Fourier series expansion and equation (2.6), this is why Fourier series have been traditionally used to compute the weight  $a_i$ , and displays them [51].

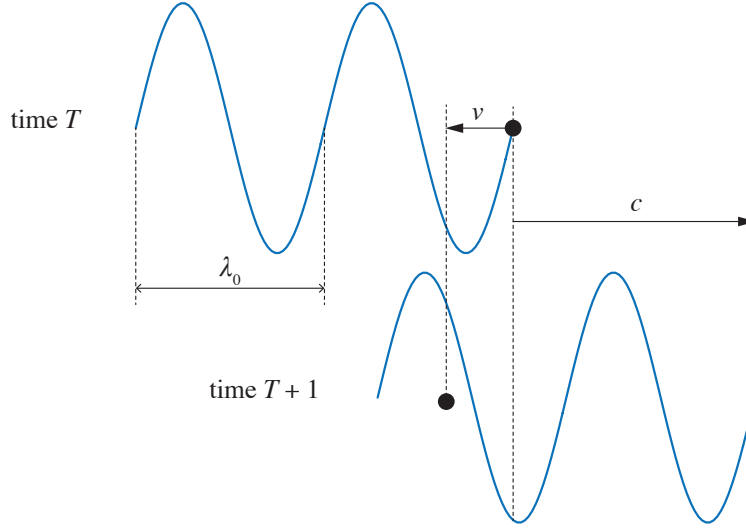


Figure 2.8: Illustration of the Doppler effect. Adapted from Aaslid (1986) [111].

**2.3.2.2 Blood Flow Velocity Estimation** Another critical point of this technology is to estimate the blood-flow velocity. To do that, two approaches are widely used: the quadrature demodulation and the Hilbert transformation [118].

The quadrature demodulation technique is illustrated in Figure 2.10. The signal received by the Doppler probe, if the contribution of a single erythrocyte is considered, is a pulsed sinusoid. It can thus be written as the windowing of a cosine function [118]:

$$s(t) = w(t) \cos(2\pi f \cdot t) \quad (2.7)$$

where  $w(t)$  is a window function.

And if we ignore the low pass filters, one can write:

$$s_*(t) = s(t) [\cos(2\pi f_{em} \cdot t) - j \sin(2\pi f_{em} \cdot t)] = w(t) \cos(2\pi f \cdot t) \cdot e^{-j2\pi f_{em} \cdot t} \quad (2.8)$$

Using Euler's formula for cosine, the equation above becomes:

$$s_*(t) = \frac{w(t)}{2} [e^{j2\pi(f-f_{em}) \cdot t} + e^{-j2\pi(f+f_{em}) \cdot t}] \quad (2.9)$$

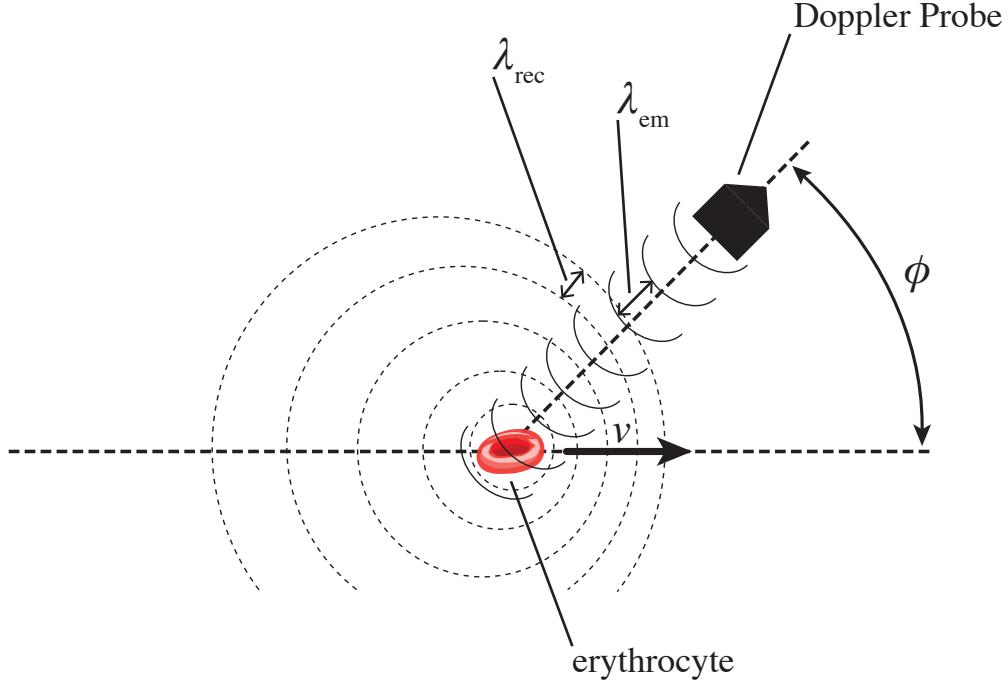


Figure 2.9: Illustration of the Doppler effect and insonation angle in the context of blood flow velocity measurement. Adapted from Deppe (2004) [51].

From this equation, we can see that one of the exponential has a high frequency component, of  $f + f_{em}$ , while the other one has a frequency component of  $f - f_{em} \triangleq \Delta f$ . Since the high frequency component are eliminated by the low pass filters, at the end of the procedure, only remain two signals, both osculating at  $\Delta f$  and in quadrature. This signal, as displayed on Figure 2.10, are considered as the real and imaginary part of a complex number, denoted as  $Q(t)$ .

Alternatively, one can use the Hilbert transform method, illustrated in Figure 2.11. The Hilbert transform is denoted as  $\mathfrak{H}$  in this thesis, is given by [119]:

$$\mathfrak{H}\{x(t)\} = \frac{1}{\pi} \int_{-\infty}^{\infty} \frac{x(\tau)}{t - \tau} d\tau \quad (2.10)$$

The resulting signal,  $Q(t)$ , is given as [118]:

$$Q(t) = w(t)e^{j2\pi \cdot \Delta f \cdot t} \quad (2.11)$$

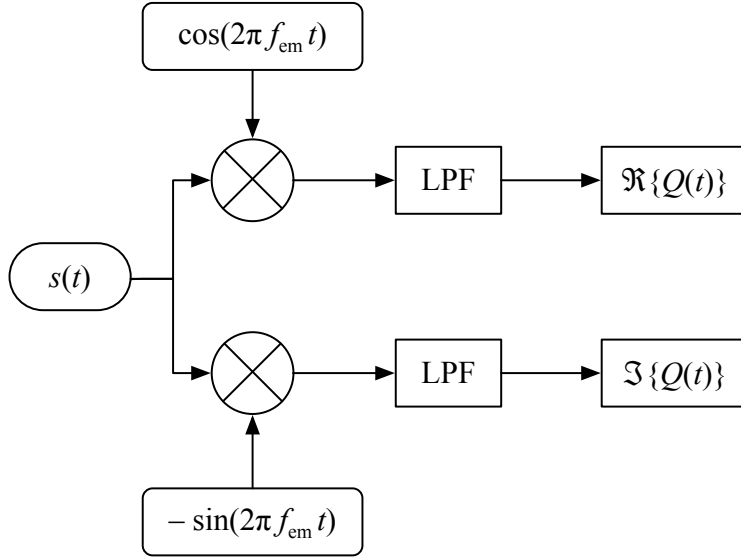


Figure 2.10: Illustration of the quadrature demodulation technique. Adapted from Azhari (2010) [118].

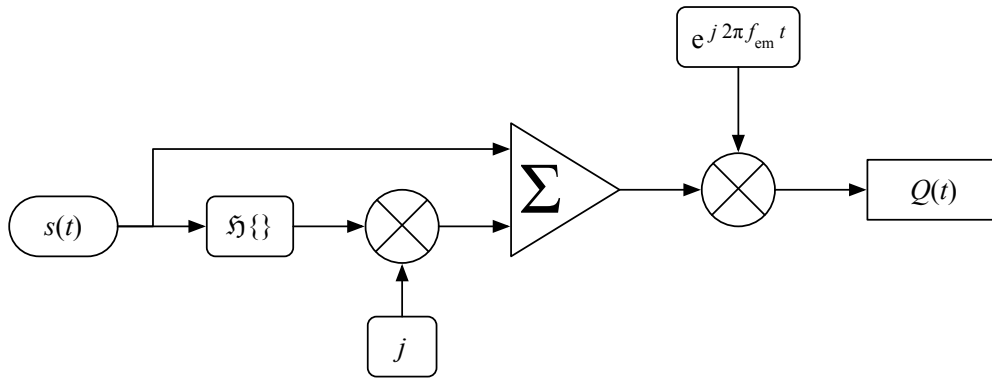


Figure 2.11: Illustration of the Hilbert transform technique. Adapted from Azhari (2010) [118].

One can then easily estimate the velocity of the signal by plugging-in equation (2.5) in equation (2.11). The results can be written as:

$$Q(t) = w(t)e^{j2\pi t \frac{2v f_{em} \cos \phi}{c}} \quad (2.12)$$

Now in the case several erythrocytes are considered, the received signal can be written as in equation (2.6), and the signal used to estimate the speed can be written as:

$$Q(t) = q_{\text{em}}(f_{\text{em}}) + w(t) \sum_i \kappa_i \times q_i(t) \quad (2.13)$$

where  $q_i(v_i, t)$  is the signal obtained by the reflection on the  $i$ th erythrocyte. Please note that these component can have different phases, but that does not influence the frequency of the contribution.

The weights of the contributions,  $\kappa_i$ , can be determined using a Fourier transform, for the same reasons as specified above.

## 3.0 METHODOLOGY

### 3.1 DATA ACQUISITION

For this preliminary data collection, eleven participants were recruited (4 females and 7 males, ages ranging from 19 to 23 years). None of these subjects had history of concussion, heart murmurs, migraines, strokes or other brain and gait conditions. Participants were asked to signed the University of Pittsburgh Institutional Review Board approved consent form and were explained the procedure prior to the beginning of the experiment and data collection.

The participants were briefed to walk at a pace of 2 mph on the Noraxon SciFit treadmill, displayed on Figure 3.1, and to remain thought-free during this 6 minutes baseline testing period. Upon the completion of this trial, the participants were asked to count backwards from 10,000 in decrements of 7 while walking for 6 minutes for another trial referred as cognitive. Approximately one week later, each participant repeated the experiment.

To observe stride time, Noraxon SciFit treadmill using capacitive sensor technology to analyze individual foot pressure (ranging from 1 to 120 N/cm<sup>2</sup>) was used at a sampling frequency of 100 Hz. The treadmill data was recorded and extracted using the manufacturer’s software.

A SONARA TCD System (Carefusion, San Diego, CA, USA), displayed on Figure 3.1, was used to measure blood-flow velocity in the mid-cerebral artery. Two 2 MHz transducers were used to gather simultaneous bilateral CBFV acquisitions from the left-MCA and right-MCA. The transducer were planted on transtemporal windows [120] to reach the MCA blood-flows. The position, angle and insonation depth of transducers were adjusted in order to get a correct MCA signal [91, 121]. Once these adjustment were performed, the transducers were fixed with a headset on both sides of the subject’s head. The data was extracted as audio

files sampled at 44.1 kHz, representing the cerebral blood flow from the R-MCA and L-MCA. These signals were resampled at 8,820 Hz (factor 5) to increase the feature extraction's speed. The down-sampled signals, referred as raw signals, are composed of multiple sinusoidal components due to the parabolic speed CBFV distribution [51]. In this study, these raw CBFV along with the envelope of the CBFV were collected. The raw signals are composed of the various velocities of blood particles in cerebral arteries and envelope signals constitute the maximal Doppler shift [51, 122].

Furthermore, the end-tidal carbon dioxide  $ETCO_2$  (BCI Capnocheck Sleep Capnograph, Smiths Medical, Waukesha, Wisconsin, USA) was monitored along with respiration rate, electrocardiogram, head movement and skin conductance via a multi-system physiological data monitoring system (Nexus-X, Mindmedia, Netherlands).



Figure 3.1: TCD System (a) and treadmill (b) used for the data collection

### 3.2 ANALYSIS OF STRIDE INTERVAL TIME SERIES

The mean, standard deviation, coefficient of variation (which is the ratio of the standard deviation to the mean) and the spectral exponent were estimated for stride interval time series extracted from both feet.

To determine the spectral exponents of the stride interval signals, the average wavelet coefficient (AWC) method was used. This method can be summarized as follows [102, 123]:

1. The wavelet transform of the centered version of the signal,  $WV_x(\tau, s)$ , is computed using the Daubechies 12 wavelet.
2. The mean average with respect to translation coefficient  $\tau$  of the magnitude of the wavelet transform is evaluated for each scale. This quantity is called:

$$WV_x(s) = \langle |WV_x(\tau, s)| \rangle_\tau \quad (3.1)$$

3. The log-log plot of  $WV_x(s)$  as a function of the scale  $s$  is plotted. The linear regression of the resulting graph is computed. The slope of this line is  $H_{fBm} + 1/2$  [102].
4. The spectral exponent  $\beta$  is evaluated using the expression:

$$\beta = 2H_{fBm} + 1 \quad (3.2)$$

The number of scales were chosen with respect of the signal length, using the following expression:

$$\text{number of scales} = 2^n \text{ with } n = \min \left[ \max \left( \left\lfloor \log_2 \left( \frac{\text{length}(x)}{4} \right) \right\rfloor, 7 \right), 3 \right] \quad (3.3)$$

where  $\lfloor \cdot \rfloor$  is the floor function,  $\text{length}(x)$  is the number of discrete samples of the signal  $x$  and  $\log_2(\cdot) = \ln(\cdot)/\ln(2)$ .

### 3.3 ANALYSIS OF MCA SIGNALS

#### 3.3.1 Statistical features

In this study, four distinct statistical features were evaluated. The standard deviation, the skewness, the kurtosis along with the cross-correlation coefficient of right and left MCA signals were extracted and compared. The first three parameters characterize the shape of the signal's distribution [124], while the last one characterizes the similarity between two signals.

Herein below, the discrete signal is called  $\mathbf{x} = [x_1, \dots, x_n]$ .

The kurtosis of a distribution can be expressed as [124]:

$$\beta_2 = \frac{\frac{1}{n} \sum_{i=1}^n (x_i - \mu)^4}{\left[ \frac{1}{n} \sum_{i=1}^n (x_i - \mu)^2 \right]^2} \quad (3.4)$$

where  $\mu$  is the mean of the signal and  $n$  is its length.

The the expression of the skewness is [124]:

$$\beta_1 = \frac{\frac{1}{n} \sum_{i=1}^n (x_i - \mu)^3}{\sqrt{\left[ \frac{1}{n} \sum_{i=1}^n (x_i - \mu)^2 \right]^3}} \quad (3.5)$$

In this study, similarity between right MCA and left MCA signals was calculated as follows [125]:

$$\text{CC}_{X|Y} = \frac{1}{n} \sum_{i=1}^n x_i y_i \quad (3.6)$$

where  $X$  and  $Y$  represent signals from the right and the left side of the MCA.

### 3.3.2 Information-theoretic features

With regard to the information-theoretic feature space, the Lempel-Ziv complexity (LZC), which represents the amount of new pattern formation in finite time sequences built upon the original signal (which can be interpreted as the randomness, the predictability and the regularity of a given discrete-time signal) [126] and the entropy rate, which represent the statistic degree of recurrence of patterns in a stochastic process [127].

In order to obtain a finite time sequence to compute the LZC, the signal is divided into  $\alpha$  finite equal spaces using  $\alpha - 1$  threshold values given as  $T_h | h \in \{1, \dots, \alpha - 1\}$  [128].

Then, portions of the quantized signal  $X_1^n = \{x_1, x_2, \dots, x_n\}$  are assembled to shape blocks such that [129]:

$$X_j^\ell = \{x_j, x_{j+1}, \dots, x_\ell\}, 1 \leq j \leq \ell \leq n | j, \ell \in \mathbb{Z}^+ \quad (3.7)$$

where the length of each block is given as  $L = j - l + 1$ , and the length of the signal is  $n$ . The blocks are a time series of successive data.

Then, for each length  $L$ , an analyse of each block is performed the following way: a counter  $c(j)$  is defined to illustrate the amount of new pattern formation. If the sequence represented in a block has not appeared in a previous analysis, this counter is incremented by one.

Eventually, the LZC is computed as given herein bellow:

$$\text{LZC} = \frac{c(n) \log_\alpha(n)}{n} \quad (3.8)$$

where  $c(n)$  is the value that the counter takes when the entire analysis is performed and  $\alpha$  represents the total number of quantized levels in the signal, chosen such as  $\alpha = 100$  in that study.

To compute the entropy rate  $\rho$  of a given stochastic process, the pattern distribution is first normalized to feature zeros mean and unit variance. This distribution is then quantized using 10 equally divided discrete amplitude levels, taking integer values between 0 and 9. The quantized distribution  $\tilde{X} = \{\tilde{x}_1, \tilde{x}_2, \dots, \tilde{x}_n\}$  is then decomposed into blocks comprised of successive samples, with length  $L$  such that  $10 \leq L \leq 30$ ,  $L \in \mathbb{Z}^+$ .

Subsequently, the distribution made up of the different blocks was encoded into  $\Omega_L = \{\omega_1, \omega_2, \dots, \omega_{n-L+1}\}$  such as [130]:

$$\omega_i = 10^{L-1} \times \tilde{x}_{i+L-1} + 10^{L-2} \times \tilde{x}_{i+L-2} + \dots + 10^0 \times \tilde{x}_i \quad (3.9)$$

with  $w_i$  varying from 0 to  $9 \times (1 - 10^L)/(1 - 10) = 10^L - 1$ .

The Shannon entropy  $S(L)$ , which represents the degree of complexity of  $\Omega_L$ , is defined by [130]:

$$S(L) = \sum_{j=1}^{10^L-1} p_{\Omega_L}(j) \ln p_{\Omega_L}(j) \quad (3.10)$$

where  $p_{\Omega_L}(j)$  is the probability of the value  $j$  in  $\Omega_L$ , which is approximated by its sample frequency in this study.

The normalized conditional entropy is then given as [131]:

$$N(L) = \frac{S(L) - S(L-1) + S(1) \times \text{pe}_{\%}(L)}{S(1)} \quad (3.11)$$

where  $S(1) \cdot \text{pe}_{\%}(L)$  is a correction term defined by the multiplication of the percentage of patterns with length  $L$  arising only once in  $\Omega_L$ ,  $\text{pe}_{\%}(L)$ , with  $S(1)$  the conditional entropy estimation of the process with unit length  $L$ , which is the Shannon entropy of white Gaussian noise process. This term corrects the underestimation of  $S(L) - S(L-1)$  for large lengths  $L$  [132]. Considering the opposite nature of the variation of the terms in the denominator (the first term decreases with  $L$  while the second term increases), the function  $N(L)$  exhibits a minimum  $\min_L [N(L)]$ . This minimum is the best estimation of the normalized conditional entropy, and it can be seen as an indicator of complexity of the process. Conversely, the complement to one of this indicator, given as  $\rho = 1 - \min_L [N(L)]$ , is an index of regularity of the stochastic process, ranging between 0 and 1 [131].

For comparison between two probability density functions purposes, one can use the cross-entropy rate. This index quantifies the amount of mutual information between two given distributions, and aims to predict the data of a considered signal using the previous and current information found in another signal. The two distributions  $X$  and  $Y$  were normalized and quantized similar to the one used to compute the entropy rate, giving as a result the two quantized distribution  $\tilde{X} = \{\tilde{x}_1, \tilde{x}_2, \dots, \tilde{x}_n\}$  and  $\tilde{Y} = \{\tilde{y}_1, \tilde{y}_2, \dots, \tilde{y}_n\}$ .

Eventually, the cross-entropy rate  $\Omega_L^{X|Y}$ , which is the information amount that can be found in one of the samples of the quantized process  $\tilde{X}$  when a pattern of  $L - 1$  samples of the quantized signal  $\tilde{Y}$  is assumed, was encoded using the following code [131]:

$$\omega_i^{X|Y} = 10^{L-1} \times \tilde{x}_{i+L-1} + 10^{L-2} \times \tilde{y}_{i+L-2} + \cdots + 10^0 \times \tilde{y}_i \quad (3.12)$$

where  $S_X(L)$ ,  $S_Y(L)$  and  $S_{X|Y}$  are the Shannon entropies of the distributions  $X$ ,  $Y$  and  $\Omega_L^{X|Y}$ .

The normalized cross-entropy was then computed as:

$$\text{NC}_{X|Y}(L) = \frac{S_{X|Y}(L) - S_Y(L - 1) + S_X(1) \times \text{pe}_{X|Y}(L)}{S_X(1)} \quad (3.13)$$

where  $\text{pe}_{X|Y}(L)$  is the percentage of arrangements of length  $L$  that were present only once in  $\Omega_L^{X|Y}$  and  $S_X(1) \cdot \text{pe}_{X|Y}(L)$  is a corrective term added for the same reasons as the one stated herein above. Similarly to the previously given algorithm,  $S_X(1)$  is the conditional entropy estimation of the stochastic process  $X$  for a unit length. The function  $\text{NC}_{X|Y}(L)$  features a minimum  $\min_L [\text{NC}_{X|Y}(L), \text{NC}_{Y|X}(L)]$ . The synchronization index is then defined by:

$$\Lambda_{X|Y} = 1 - \min_L [\text{NC}_{X|Y}(L), \text{NC}_{Y|X}(L)] \quad (3.14)$$

and it ranges from 0 (when  $X$  and  $Y$  are independent) to 1 (when  $X$  and  $Y$  are synchronized stochastic processes).

### 3.3.3 Frequency features

Features were also extracted with regard to the frequency domain: the peak frequency, spectral centroid and bandwidth were computed as characterization indexes for the extracted from the TCD signals [122].

The peak frequency, given as  $f_p$ , is the frequency location where the largest spectral power can be found, and it is thus computed as:

$$f_p = \operatorname{argmax}_{f \in [0, f_{\max}]} \{|F_X(f)|^2\} \quad (3.15)$$

where  $F_X(f)$  is the Fourier transform of the signal  $X$  and  $f_{\max}$  the spectrum's maximum frequency, equal to the sampling frequency divided by two.

The spectral centroid,  $f_c$ , can be interpreted as the spectrum's center of mass and is calculated as follows [133]:

$$f_c = \frac{\int_0^{f_{\max}} f |F_X(f)|^2 df}{\int_0^{f_{\max}} |F_X(f)|^2 df} \quad (3.16)$$

The bandwidth  $BW$ , representing the dispersion of the spectrum, was computed as [122]:

$$BW = \sqrt{\frac{\int_0^{f_{\max}} (f - f_c)^2 |F_X(f)|^2 df}{\int_0^{f_{\max}} |F_X(f)|^2 df}} \quad (3.17)$$

Please note that in this study, all of the features were implemented as:

$$\int_{t_1}^{t_2} x(t) dt \approx \sum_{n=n_1}^{n_2-1} x[n] T_{\text{samp}} \quad (3.18)$$

where  $n_1$  and  $n_2$  correspond to  $t_1$  and  $t_2$ , and  $T_{\text{samp}}$  is the sampling frequency. Please note that  $x(t)$  denotes a continuous time signal while  $x[n]$  is in the discrete time domain.

### 3.3.4 Time-frequency features

Even though the Fourier transform is a powerful tool to access the frequency content of a signal, it might be ill-fitted for the study of non-stationary signals [134]. To tackle this issue, tools have been developed to examine the evolution of the frequency content of a signal over time. One of the first and simplest development in that area is the short time Fourier transform (STFT) [135]. The basic idea behind this concept is to compute and combine Fourier transforms of windowed section of a signal. However, in this method, a fixed window length is used, and numerous problems such as the complexity of the determination of the optimal window or the fixed, lower bounded time-frequency resolution size might appear [136]. The lower bound of the STFT resolution is given by [136]:

$$\Delta t \Delta f \geq \frac{1}{4\pi} \quad (3.19)$$

where  $\Delta t$  and  $\Delta f$  are respectively the time and frequency resolution.

To tackle these limitations, a frequency varying distribution known as the wavelet transform was introduced. The idea behind this tool is to change the frequency resolution as the frequency changes, using scaled and shifted versions of the window, also called mother wavelet. This transform is given by [136]:

$$\mathfrak{W}\{x(t)\}(s, \tau) = \frac{1}{\sqrt{s}} \int_{-\infty}^{\infty} x(t) \cdot \psi^* \left( \frac{t - \tau}{s} \right) dt \quad (3.20)$$

where  $s$  is the scaling parameter,  $\tau$  is the shifting,  $(\cdot)^*$  is the complex conjugate and  $\psi(\cdot)$  the mother wavelet.

However, the computational complexity of this transform is high because of the redundant information present in terms of scaling [137]. To reduce the redundancy of the transform, a solution is to make the scale and translation parameters discrete [137, 138]:

$$\psi_{j,k}(t) = \frac{1}{\sqrt{2^j}} \psi \left( \frac{t - k2^j}{2^j} \right) = 2^{-j/2} \psi(2^{-j}t - k) \quad (3.21)$$

The Mallat algorithm [139], which is used to compute discrete wavelet transform, is based on the projection of the signal on a set of approximation and detail subspaces [137]:

$$x(t) = \sum_k a_j[k] 2^{-j/2} \varphi(2^{-j}t - k) + \sum_k d_j[k] 2^{-j/2} \psi(2^{-j}t - k) \quad (3.22)$$

where  $\varphi(\cdot)$  is called scaling function, and is related to the approximation coefficients  $a_j(k)$ , and  $d_j(k)$  are the detail coefficients.

The coefficients are given as [137]:

$$\begin{cases} a_j[k] = \langle x(t), \varphi_{j,k}(t) \rangle = \int x(t) 2^{-j/2} \varphi^*(2^{-j}t - k) dt \\ d_j[k] = \langle x(t), \psi_{j,k}(t) \rangle = \int x(t) 2^{-j/2} \psi^*(2^{-j}t - k) dt \end{cases} \quad (3.23)$$

Now, considering that the scale and wavelet functions can be written as:

$$\begin{cases} \varphi(t) = \sqrt{2} \sum_k h[k] \cdot \varphi(2t - k) \\ \psi(t) = \sqrt{2} \sum_k g[k] \cdot \psi(2t - k) \end{cases} \quad (3.24)$$

Where the coefficients  $h[k]$  and  $g[k]$  can be computed as [137]:

$$\begin{cases} h[k] = \langle \varphi(t), \sqrt{2} \varphi(2t - k) \rangle \\ g[k] = \langle \psi(t), \sqrt{2} \varphi(2t - k) \rangle \end{cases} \quad (3.25)$$

where  $h[k]$  and  $g[k]$  are respectively a low-pass and high-pass filter.

The approximation coefficients captures the low-frequency content of the signal, while the detail coefficients allow retrieving high frequency information on the signal. The coefficients can be computed recursively using:

$$\begin{cases} a_j[k] = \sum_m h[m - 2k] \cdot a_{j-1}[m] \\ d_j[k] = \sum_m g[m - 2k] \cdot a_{j-1}[m] \end{cases} \quad (3.26)$$

Since these expressions can be seen as the decimated responses of the signal to a low-pass and high-pass filters [140], so it can be implemented as displayed on Figure 3.2.

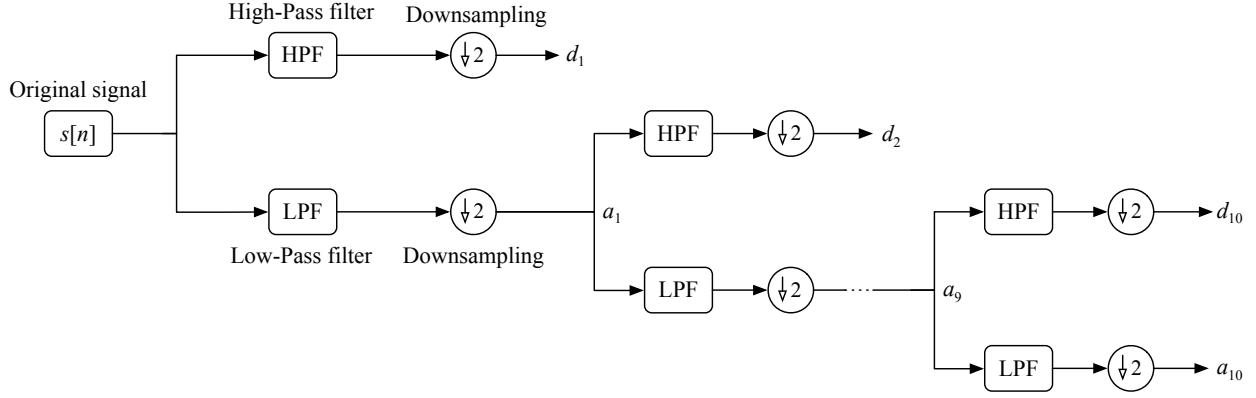


Figure 3.2: Illustration of the 10 levels discrete wavelet transform algorithm.

To extract features related to the time-scale domain, the signal was decomposed into 10 levels  $W = \{a_{10}, d_{10}, d_9, \dots, d_1\}$  (where  $a_{10}$  is the approximation coefficient and  $d_k$  represents detail coefficient at the  $k$ th level [141]) using a discrete wavelet transform approach and the Meyer wavelet, given in Figure 3.3.

The relative wavelet energy from both the approximation coefficient and detail coefficients are then computed as [142]:

$$\Xi_{a_{10}} = \frac{\|a_{10}\|^2}{\|a_{10}\|^2 + \sum_{k=1}^{10} \|d_k\|^2} \times 100 \quad (3.27)$$

$$\Xi_{d_k} = \frac{\|d_k\|^2}{\|a_{10}\|^2 + \sum_{k=1}^{10} \|d_k\|^2} \times 100 \quad (3.28)$$

where  $\|\cdot\|$  is the Euclidian norm, defined as  $\|\mathbf{x}\| = \sqrt{\sum_i x_i^2}$ ,  $\mathbf{x} = [x_1, \dots, x_n]$ .

These metrics describe the relative energies repartition within distinct frequency bands based upon the ratio of the  $k$ -th level of decomposition to the total energy of the signal.

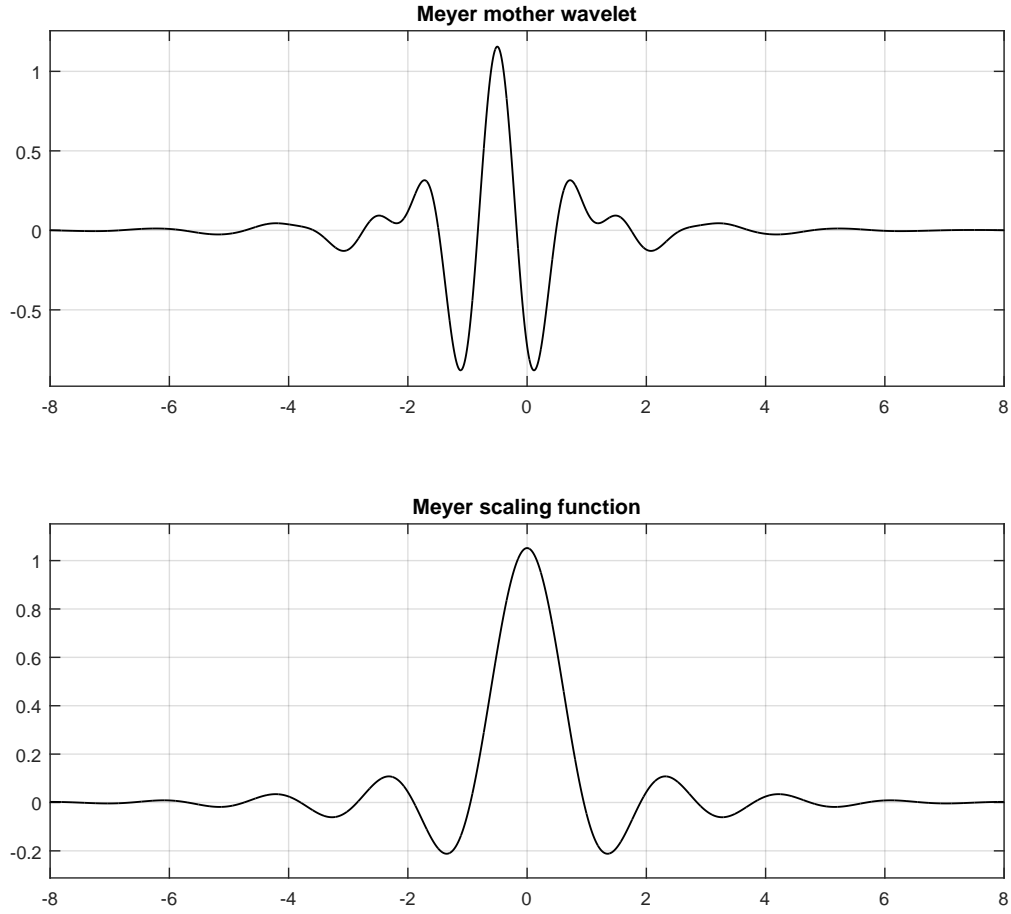


Figure 3.3: Plot of the Meyer mother wavelet.

The wavelet entropy  $\Omega$  is an indicator of the order of the decomposed signal [142]. It is a representation of the clustering of the wavelet energies comprised in the different decomposition levels.

$$\Omega = -\Xi_{a_{10}} \log_2 \Xi_{a_{10}} - \sum_{k=1}^{10} \Xi_{d_k} \log_2 \Xi_{d_k} \quad (3.29)$$

where  $\Xi$  are the relative energies defined herein above.

### 3.4 STATISTICAL TEST

The software SAS version 9.3 (SAS Institute, Inc., Cary, North Carolina) was used to conduct our statistical analysis. Our chosen approach was to consider the two trials separately, and to fit a complex enough model to accurately represent the between-trial correlation. The reason for this approach is the maximization of the use of information and statistical power. Please note that for the correlation analysis, the features were averaged between the two trials.

To explore the significance of differences in measures between the two trials, linear mixed models were fitted with the gait/blood flow measures as the dependent variable, the trial index as the factor of interest and a subject random effect accounting for numerous correlated measurements from the same participant. The SAS MIXED procedure was used.

Then, the difference between the baseline trials and cognitive trials were calculated for each feature, and similar mixed models were fitted with the difference as the dependent variable, but in an intercept-only model to retrieve statistical significance for the baseline vs cognitive difference under two correlated trials.

Next, the effect of the participant characteristics was considered. Another series of models were fitted, with each features under each condition as the dependent variable, each participant characteristic as the factor of interest and a participant random effect accounting for multiple trials.

Eventually, the correlation coefficients across gait and blood flow measures were examined. The first step was to average the measures across two trials in the same condition, and the Pearson correlation coefficients between the gait and blood flow measures and between the left and right side signals of blood flow velocity features were then computed. Additionally, partial correlations adjusted for the participant characteristics were calculated.

Because of the large number of measures and statistical tests performed in our analysis, false discovery rate (FDR) methodology to adjust  $p$ -values for multiplicity was used [143].

## 4.0 RESULTS

The end-tidal carbon dioxide level does not influence the mean diameter of the middle cerebral arteries [66]. Consequently, it is not taken into consideration. The results are presented in tables in the form of (mean  $\pm$  standard deviation) where the baseline period is pointed out by an “B” and the cognitive task is indicated by a “C”. R-MCA indicates the right MCA, while L-MCA indicates the left MCA. The test-retest were not found to introduce statistical differences if the FDR adjusted  $p$ -values are considered.

### 4.1 STRIDE INTERVAL FEATURES

Feature extracted from the subjects’ stride intervals are provided in Table 4.1. No statistical differences between the baseline (denoted as “B”) and cognitive states (denoted as “C”) were found if the FDR adjusted  $p$ -values are considered.

Table 4.1: Stride interval features.\* denotes a multiplication by  $10^{-2}$ .

		Right foot	Left foot
Mean (s)	B	$1.24 \pm 0.07$	$1.24 \pm 0.07$
	C	$1.26 \pm 0.07$	$1.26 \pm 0.07$
Coefficient of variation	B	$(3.09 \pm 0.97)^*$	$(2.89 \pm 0.76)^*$
	C	$(2.76 \pm 1.17)^*$	$(2.44 \pm 0.82)^*$
Spectral exponent $\beta$	B	$0.64 \pm 0.49$	$0.66 \pm 0.42$
	C	$0.41 \pm 0.27$	$0.47 \pm 0.22$

## 4.2 MCA SIGNAL FEATURES

### 4.2.1 Time features

Table 4.2 summarizes time-domain feature values for the raw and the envelope signals. For every metric considered in that table, no statistical differences between the left side and the right side were observed. However, statistical differences between cognitive state and baseline state were observed for the standard deviation of the envelope signal ( $p \approx 0.018$ ) for both R-MCA and L-MCA, and for both the envelope and raw signals' R-MCA and L-MCA cross-correlation ( $p \approx 0.018$ ).

Table 4.2: Time features from raw and envelope CBFV signals. \* denotes a multiplication by  $10^{-3}$ . † denotes FDR corrected statistical differences between baseline and cognitive runs.

		RAW		ENVELOPE	
		R-MCA	L-MCA	R-MCA	L-MCA
Standard Dev.	B	$0.13 \pm 0.10$	$0.13 \pm 0.08$	$3.77 \pm 1.01^\dagger$	$4.03 \pm 1.13^\dagger$
	C	$0.15 \pm 0.10$	$0.14 \pm 0.08$	$5.02 \pm 1.62^\dagger$	$5.44 \pm 1.36^\dagger$
Skewness	B	$(-4.99)^* \pm 0.02$	$(-1.52)^* \pm 0.01$	$-1.03 \pm 0.74$	$-0.80 \pm 0.76$
	C	$(-7.15)^* \pm 0.02$	$(-0.11)^* \pm 0.03$	$-1.22 \pm 0.82$	$-1.07 \pm 0.75$
Kurtosis	B	$4.38 \pm 2.74$	$5.08 \pm 3.31$	$5.50 \pm 3.95$	$4.73 \pm 3.13$
	C	$4.51 \pm 1.67$	$5.11 \pm 3.22$	$5.41 \pm 2.98$	$4.47 \pm 1.91$
Cross-Corr.	B	$(7.27 \pm 2.04)^*\dagger$		$0.98 \pm 0.01^\dagger$	
	C	$0.02 \pm 0.02^\dagger$		$0.97 \pm 0.02^\dagger$	

### 4.2.2 Information-theoretic features

Information-theoretic features from both CBFV raw and envelope signals are presented in Table 4.3. The LZC and synchronization index of the envelope signals exhibited significant statistical differences between the two states ( $p < 0.02$ ).

Table 4.3: Information-theoretic features from raw and envelope CBFV signals. \* denotes a multiplication by  $10^{-3}$ . † denotes FDR corrected statistical differences between baseline and cognitive runs.

		RAW		ENVELOPE	
		R-MCA	L-MCA	R-MCA	L-MCA
LZC	B	$0.71 \pm 0.04$	$0.71 \pm 0.04$	$0.70 \pm 0.02^\dagger$	$0.70 \pm 0.02^\dagger$
	C	$0.70 \pm 0.04$	$0.70 \pm 0.03$	$0.68 \pm 0.02^\dagger$	$0.68 \pm 0.03^\dagger$
Entropy rate	B	$0.09 \pm 0.10$	$0.10 \pm 0.15$	$(7.61 \pm 1.75)^*$	$(7.56 \pm 2.43)^*$
	C	$0.11 \pm 0.13$	$0.11 \pm 0.11$	$0.01 \pm 0.01$	$0.01 \pm 0.01$
Synchronization index	B	$0.17 \pm 0.13$		$0.07 \pm 0.03^\dagger$	
	C	$0.16 \pm 0.12$		$0.12 \pm 0.06^\dagger$	

### 4.2.3 Frequency features

Table 4.4 summarizes the frequency characteristics of raw and envelope signals. These metrics do not display any significant statistical differences between the left and right MCA raw and envelope signals. The spectral centroid of the R-MCA raw signal was found to feature statistical differences ( $p = 0.038$ ), while the bandwidth of the raw CBFV shows statistical differences for the L-MCA, with  $p < 0.01$ .

### 4.2.4 Time-frequency features

Table 4.5 shows the wavelet entropy values for raw and envelope signals, while Figure 4.1 displays the wavelet decomposition of the raw CBFV signal. In the case the wavelet entropies are considered, the R-MCA and L-MCA CBFV wavelet entropies feature statistical differences between baseline and cognitive states, with respectively  $p = 5.4 \cdot 10^{-3}$  and  $p = 1.1 \cdot 10^{-2}$ .

Figure 4.1 exhibits that the majority of wavelet energy is massed in high order detail coefficients (mainly for  $7 \leq k \leq 10$ ,  $k \in \mathbb{Z}^+$ ). Statistical differences between the baseline and cognitive state can be found in the bands  $d_{10}$  and  $d_8$  for the raw R-MCA and L-MCA signals ( $p \leq 0.03$ ).

Table 4.4: Frequency features from raw and envelope CBFV signals (values are in Hertz). <sup>†</sup> denotes FDR corrected statistical differences between baseline and cognitive runs.

		RAW		ENVELOPE	
		R-MCA	L-MCA	R-MCA	L-MCA
Spectral Centroid	B	$546 \pm 47.3^\dagger$	$523 \pm 62.1$	$2.92 \pm 0.43$	$2.91 \pm 0.40$
	C	$504 \pm 80.6^\dagger$	$488 \pm 68.2$	$2.80 \pm 0.46$	$2.72 \pm 0.49$
Peak frequency	B	$574 \pm 115$	$539 \pm 144$	$1.25 \pm 0.62$	$1.08 \pm 0.71$
	C	$437 \pm 202$	$421 \pm 196$	$0.84 \pm 0.81$	$0.71 \pm 0.84$
Bandwidth	B	$172 \pm 15.8$	$174 \pm 12.4^\dagger$	$2.38 \pm 0.33$	$2.40 \pm 0.30$
	C	$186 \pm 16.1$	$193 \pm 17.7^\dagger$	$2.43 \pm 0.24$	$2.37 \pm 0.21$

Table 4.5: Wavelet entropy values for raw and envelope CBFV signals. <sup>†</sup> denotes FDR corrected statistical differences between baseline and cognitive runs.

		RAW		ENVELOPE	
		R-MCA	L-MCA	R-MCA	L-MCA
$\Omega$	B	$1.02 \pm 0.21^\dagger$	$1.11 \pm 0.27^\dagger$	$0.03 \pm 0.02$	$0.04 \pm 0.03$
	C	$1.22 \pm 0.23^\dagger$	$1.32 \pm 0.23^\dagger$	$0.05 \pm 0.06$	$0.06 \pm 0.03$

Figure 4.2 displays that entirety of wavelet energy is massed in the approximation coefficient ( $a_{10}$  accounts for 99% of the energy).

#### 4.2.5 Correlation between left and right MCA blood flow

Statistical significance for the correlation between the left and right MCA CBFV are only found for the wavelet decomposition of the raw CBFV signals: the levels  $d_5$  to  $d_7$  exhibit a correlation coefficient greater than 0.8 with  $p \leq 0.005$ . The levels  $d_2$  and  $d_1$  feature a correlation coefficient greater than 0.9 with  $p \ll 0.001$ .

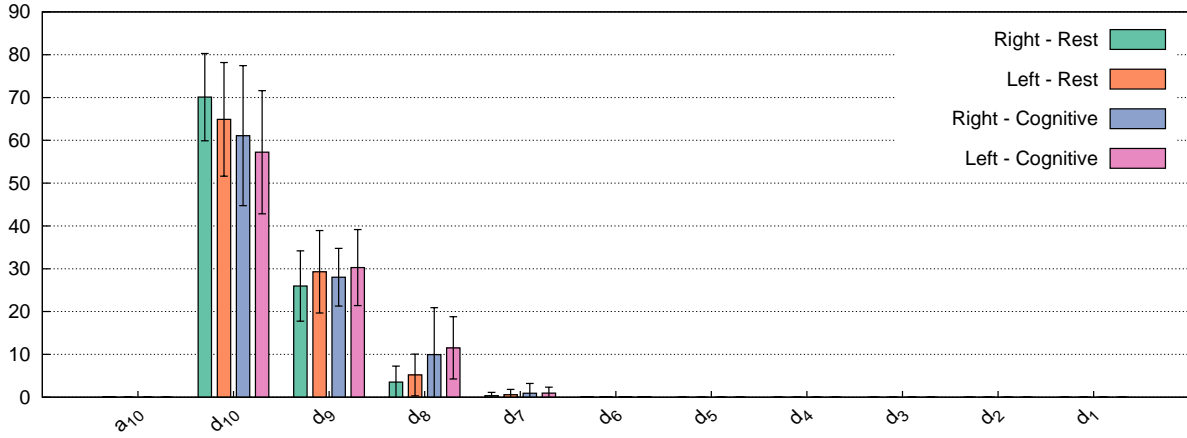


Figure 4.1: The 10 level wavelet decomposition of raw signals

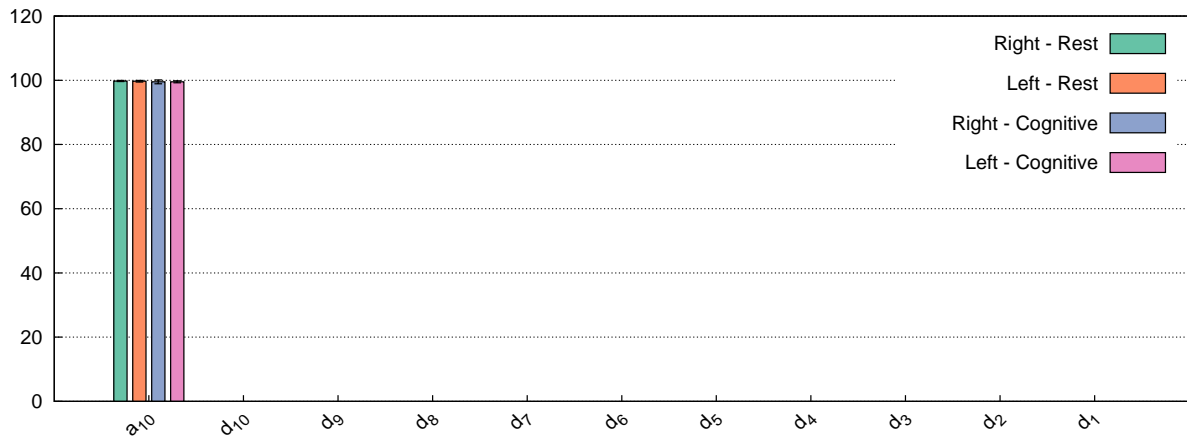


Figure 4.2: The 10 level wavelet decomposition of envelope signals

### 4.3 CORRELATION BETWEEN GAIT AND MCA FEATURES

The Pearson correlation coefficient  $\rho$  were thresholded using the following rule:

$$\rho_{th} = \begin{cases} 1 & \text{if } |\rho| > 0.7 \text{ and } p < 0.05 \\ 0 & \text{otherwise} \end{cases} \quad (4.1)$$

Figure 4.3 displays the correlation of the gait features and the CBFV features. From this figure, it is clear that with the cognitive processing added task there was a greater number of correlated gait and blood flow velocity features: in the baseline test, 9.1% of the potential relations between gait and cerebral blood flow were correlated, while in the cognitive processing added task condition, 14.5% of the potential gait and blood flow measures were related.

More specifically, all the stride-related features except the right foot spectral exponent coefficient are found to be correlated with at least one feature extracted from the cerebral blood flow signals. Indeed, 4 blood flow related features are found to be correlated to both the left and right feet mean stride interval (peak frequency of the R-MCA raw signal, standard deviation of the L-MCA raw signal, both the skewness and kurtosis of the R-MCA envelope signals). The standard deviation and coefficient of variation of the right foot stride interval both are correlated with 10 of the features of the CBFV (with 9 of the correlated being the same for the left and right foot). The same stride related features when the left foot is considered are correlated with 11 and 10 features of the CBFV, respectively. Lastly, the spectral exponent coefficient for the left foot stride interval is correlated to two of the central blood flow velocity signals features: the R-MCA raw signal peak frequency and the R-MCA envelope signal wavelet entropy.

#### 4.4 IMPACT OF ANTHROPOMETRIC VARIABLES ON FEATURES

The anthropometric variables were not found to have an impact on any of the features.

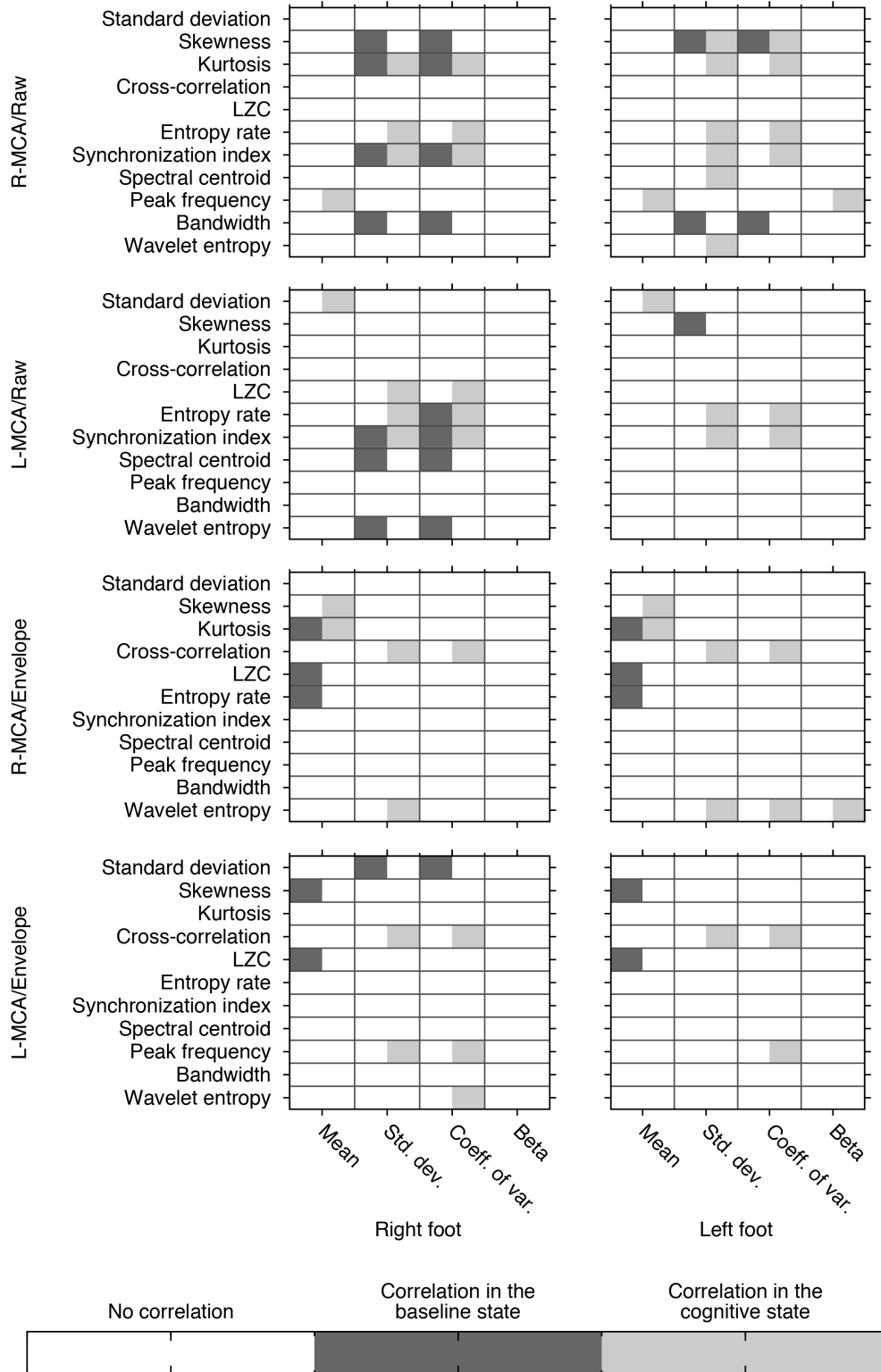


Figure 4.3: Correlation and adjusted correlation in the baseline and cognitive states.

## 5.0 DISCUSSION AND LIMITATIONS

### 5.1 DISCUSSION

Our major finding is that there are statistical differences in cerebral blood flow velocities in MCA between the baseline and cognitive states during walking. These differences were observed both in the raw signals and in the envelope signals (i.e., the maximal velocities) associated with cerebral blood flow velocities.

The statistical differences revealed in this study between blood flow during walking and blood flow during walking with an added cognitive processing task illustrate the suggested performance pattern seen in older adults with greater difficulty walking under challenging conditions such as walking and talking or walking and thinking. Under the challenge of the added cognitive task, it was more difficult to maintain usual gait performance. The difficulty manifested in gait as largely greater inconsistency in the pattern of strides than in the mean of the stride interval time series. This difficulty was also mirrored in the cerebral blood flow. Thus under the cognitive processing task condition, the range of gait performance was expanded for some variables, despite no change in the group mean for the gait characteristics. The expanded range of gait performance may underlie the different and greater number of correlations between gait and blood flow in the walking plus cognitive processing condition. A cognitive challenging task during walking may alter the range of gait performance, which is also associated with greater cerebral blood flow or ‘work’ of the brain.

Among the stride measures, the standard deviation of the stride interval exhibited the strongest correlation with blood flow velocity features. This finding may indicate that while the cognitive processing did not disrupt gait described by the mean of the stride interval, the added cognition may have influenced the consistency of gait performance (eg, standard

deviation). While all participants accomplished the task of walking and thinking on the treadmill with no change in the mean stride characteristics, the difference in the level of cognitive challenge for participants was apparent in the inconsistency of gait. The greater cognitive challenge for some was associated with greater blood flow. The lack of statistical differences between the first and second trials denotes that the extracted features tend to be trial-independent.

The lack of statistical differences between the first and second trials denotes that the extracted features tend to be trial-independent.

## **5.2 LIMITATIONS OF THE STUDY**

A potential limitation of this study comes from the fact that the participants were instructed to walk on a treadmill: indeed, changes in the gait characteristics are very likely concealed by the walking rhythm induced by the treadmill.

## 6.0 CONCLUSIONS AND FUTURE WORK

### 6.1 CONCLUSIONS

In this thesis, the dual task methodology exhibited that the cerebral blood flow velocity signals in the baseline and cognitive states during walking are statistically different. These differences can be found in extracted features for both the raw and envelope of the L-MCA and R-MCA central blood flow velocity signals. While the changes in gait features were subtle, the different and more relations between gait and blood flow with the added cognitive processing during walking suggests cerebral blood flow velocity may represent the work of the brain when thinking and walking.

### 6.2 FUTURE WORK

Now that we exhibited that the correlation between the CBFV and the gait features changes when a cognitive process is performed, an interesting direction would be to build a mobile multi-system gait monitoring platform to access the effect of a cognitive load on other physiological parameters in a real-world environment.

Then, data collection in a dual-task context using this device could be realized on a wide panel of participants, and potential differences between the cognitive and baseline states, along with some potential machine learning application in order to determine the state of a patient could be investigated. This would allow notifying patients from a potential cognitive overload resulting in a degradation of the gait characteristics, thus greatly increasing the trips and falls risks.

Moreover, collecting some data on elderly individuals to confirm our findings would be an interesting research direction. Indeed, since our findings are very encouraging considering the fact that the data was collected on healthy young adults, maybe it would lead to improved results in terms of statistical differences if older people were recruited. If differences were to be found in the gait features, that could mean that the system could be simplified and embedded on portable devices, capable of warning the subjects of an increase in the falling risk.

## BIBLIOGRAPHY

- [1] P. Sheridan, J. Solomont, N. Kowall, and J. Hausdorff, “Influence of executive function on locomotor function: divided attention increases gait variability in Alzheimer’s disease,” *Journal of the American Geriatrics Society*, vol. 51, no. 11, pp. 1633–1637, 2003.
- [2] E. Al-Yahya, H. Dawes, L. Smith, A. Dennis, K. Howells, and J. Cockburn, “Cognitive motor interference while walking: a systematic review and meta-analysis,” *Neuroscience and Biobehavioral Reviews*, vol. 35, no. 3, pp. 715–728, 2011.
- [3] Y. Lajoie, N. Teasdale, C. Bard, and M. Fleury, “Attentional demands for static and dynamic equilibrium,” *Experimental Brain Research*, vol. 97, no. 1, pp. 139–144, 1993.
- [4] R. Baker, “The history of gait analysis before the advent of modern computers,” *Gait and Posture*, vol. 26, no. 3, pp. 331–342, 2007.
- [5] L. Lee and W. E. L. Grimson, “Gait analysis for recognition and classification,” in *Proceedings of the Fifth IEEE International Conference on Automatic Face and Gesture Recognition*. Washington, DC, 20-21 May 2002, pp. 148–155.
- [6] S. Sarkar, P. J. Phillips, Z. Liu, I. R. Vega, P. Grother, and K. W. Bowyer, “The HumanID gait challenge problem: Data sets, performance, and analysis,” *IEEE Transactions on Pattern Analysis and Machine Intelligence*, vol. 27, no. 2, pp. 162–177, 2005.
- [7] D. Gafurov, K. Helkala, and T. Søndrol, “Biometric gait authentication using accelerometer sensor,” *Journal of Computers*, vol. 1, no. 7, pp. 51–59, 2006.
- [8] T. Iso and K. Yamazaki, “Gait analyzer based on a cell phone with a single three-axis accelerometer,” in *Proceedings of the 8th Conference on Human-computer Interaction With Mobile Devices and Services*. Helsinki, Finland, 1215 September 2006, pp. 141–144.
- [9] J. A. Lee, S. H. Cho, J. W. Lee, K. H. Lee, and H. K. Yang, “Wearable accelerometer system for measuring the temporal parameters of gait,” in *Proceedings of the 29th Annual International Conference of the IEEE Engineering in Medicine and Biology Society*. Lyon, France, 22-26 August 2007, pp. 483–486.

- [10] R. Moe-Nilssen and J. L. Helbostad, "Estimation of gait cycle characteristics by trunk accelerometry," *Journal of Biomechanics*, vol. 37, no. 1, pp. 121–126, 2004.
- [11] B. S. Boyd, C. Puttlitz, L. J. Noble-Haeusslein, C. M. John, A. Trivedi, and K. S. Topp, "Deviations in gait pattern in experimental models of hindlimb paresis shown by a novel pressure mapping system," *Journal of Neuroscience Research*, vol. 85, no. 10, pp. 2272–2283, 2007.
- [12] E. B. Titianova, P. S. Mateev, and I. M. Tarkka, "Footprint analysis of gait using a pressure sensor system," *Journal of Electromyography and Kinesiology*, vol. 14, no. 2, pp. 275–281, 2004.
- [13] J. M. Hausdorff, M. E. Cudkowicz, R. Firtion, J. Y. Wei, and A. L. Goldberger, "Gait variability and basal ganglia disorders: Stride-to-stride variations of gait cycle timing in Parkinson's disease and Huntington's disease," *Movement Disorders*, vol. 13, no. 3, pp. 428–437, 1998.
- [14] T. E. Hewett, F. R. Noyes, S. D. Barber-Westin, and T. P. Heckmann, "Decrease in knee joint pain and increase in function in patients with medial compartment arthrosis: a prospective analysis of valgus bracing," *Orthopedics*, vol. 21, no. 2, pp. 131–140, 1998.
- [15] R. N. Stauffer, E. Y. Chao, and A. N. Györy, "Biomechanical gait analysis of the diseased knee joint." *Clinical Orthopaedics and Related Research*, vol. 126, pp. 246–255, 1977.
- [16] U. H. Buzzi, N. Stergiou, M. J. Kurz, P. A. Hageman, and J. Heidel, "Nonlinear dynamics indicates aging affects variability during gait," *Clinical Biomechanics*, vol. 18, no. 5, pp. 435–443, 2003.
- [17] L. Sudarsky, "Geriatrics: gait disorders in the elderly." *The New England Journal of Medicine*, vol. 322, no. 20, pp. 1441–1446, 1990.
- [18] S.-E. Soh, M. E. Morris, and J. L. McGinley, "Determinants of health-related quality of life in parkinsons disease: a systematic review," *Parkinsonism and Related Disorders*, vol. 17, no. 1, pp. 1–9, 2011.
- [19] M. W. Whittle, "Clinical gait analysis: A review," *Human Movement Science*, vol. 15, no. 3, pp. 369–387, 1996.
- [20] N. V. Boulgouris, D. Hatzinakos, and K. N. Plataniotis, "Gait recognition: a challenging signal processing technology for biometric identification," *IEEE Signal Processing Magazine*, vol. 22, no. 6, pp. 78–90, 2005.
- [21] G. Johansson, "Visual perception of biological motion and a model for its analysis," *Perception and Psychophysics*, vol. 14, no. 2, pp. 201–211, 1973.

- [22] J. E. Cutting and L. T. Kozlowski, "Recognizing friends by their walk: Gait perception without familiarity cues," *Bulletin of the Psychonomic Society*, vol. 9, no. 5, pp. 353–356, 1977.
- [23] S. Stitt and Y. F. Zheng, "Distal learning applied to biped robots," in *Proceedings of the IEEE International Conference on Robotics and Automation*. San Diego, CA, 8-13 May 1994, pp. 137–142.
- [24] S. Collins, A. Ruina, R. Tedrake, and M. Wisse, "Efficient bipedal robots based on passive-dynamic walkers," *Science*, vol. 307, no. 5712, pp. 1082–1085, 2005.
- [25] S. H. Collins and A. Ruina, "A bipedal walking robot with efficient and human-like gait," in *Proceedings of the 2005 IEEE International Conference on Robotics and Automation*. Barcelona, Spain, 18-22 April 2005, pp. 1983–1988.
- [26] V. T. Inman, H. J. Ralston, and F. Todd, *Human walking*. Williams Wilkins, 1981.
- [27] R. C. Schafer, *Clinical biomechanics: musculoskeletal actions and reactions*. Williams Wilkins, 1987.
- [28] D. A. Winter, "Human balance and posture control during standing and walking," *Gait and Posture*, vol. 3, no. 4, pp. 193–214, 1995.
- [29] G. Yogev-Seligmann, J. Hausdorff, and N. Giladi, "The role of executive function and attention in gait," *Movement Disorders*, vol. 23, no. 3, pp. 329–342, 2008.
- [30] E. Fraizer and S. Mitra, "Methodological and interpretive issues in posture-cognition dual-tasking in upright stance," *Gait and Posture*, vol. 27, no. 2, pp. 271–279, 2008.
- [31] N. Giladi, "Gait and mental function: the interplay between walking, behavior and cognition," *Journal of Neural Transmission*, vol. 114, no. 10, pp. 1241–1242, 2007.
- [32] E. Martin and R. Bajcsy, "Analysis of the effect of cognitive load on gait with off-the-shelf accelerometers," in *Proceedings of the Third International Conference on Advanced Cognitive Technologies and Applications*. Rome, Italy, 25-30 September 2011, pp. 1–6.
- [33] G. Allali, M. Meulen, , and F. Assal, "Gait and cognition: the impact of executive function," *Schweizer Archiv fur Neurologie und Psychiatrie*, vol. 161, no. 6, pp. 195–199, 2010.
- [34] I. Goethals, K. Audenaert, C. Van de Wiele, and R. Dierckx, "The prefrontal cortex: insights from functional neuroimaging using cognitive activation tasks," *European Journal of Nuclear Medicine and Molecular Imaging*, vol. 31, no. 3, pp. 408–416, 2004.
- [35] M. D. Lezak, *Neuropsychological assessment*. Oxford University Press, 2004.

- [36] F. Collette, M. Hogge, E. Salmon, and M. Van der Linden, “Exploration of the neural substrates of executive functioning by functional neuroimaging,” *Neuroscience*, vol. 139, no. 1, pp. 209–221, 2006.
- [37] J. A. Alvarez and E. Emory, “Executive function and the frontal lobes: a meta-analytic review,” *Neuropsychology Review*, vol. 16, no. 1, pp. 17–42, 2006.
- [38] P. Plummer-D’Amatoa, L. Altmannb, D. Saracinoc, E. Foxd, A. Behrmand, and M. Marsiskef, “Interactions between cognitive tasks and gait after stroke: A dual task study,” *Gait and Posture*, vol. 27, no. 4, pp. 683–688, 2008.
- [39] A. Rao, U. Jasim, A. Gillman, and E. Louis, “Cognitive motor interference during dual-task gait in essential tremor,” *Gait and Posture*, vol. 38, no. 3, pp. 403–409, 2013.
- [40] J. Hollman, F. Kovash, J. Kubik, and R. Linbo, “Age-related differences in spatiotemporal markers of gait stability during dual task walking,” *Gait and Posture*, vol. 26, no. 1, pp. 113–119, 2007.
- [41] M. K. Beauchamp, K. M. Sibley, B. Lakhani, J. Romano, S. Mathur, R. S. Goldstein, and D. Brooks, “Impairments in systems underlying control of balance in COPD,” *Chest*, vol. 141, no. 6, pp. 1496–1503, 2012.
- [42] H. Axer, M. Axer, H. Sauer, O. W. Witte, and G. Hagemann, “Falls and gait disorders in geriatric neurology,” *Clinical Neurology and Neurosurgery*, vol. 112, no. 4, pp. 265–274, 2010.
- [43] T. Ijmker and C. Lamoth, “Gait and cognition: the relationship between gait stability and variability with executive function in persons with and without dementia,” *Gait and Posture*, vol. 35, no. 1, pp. 126–131, 2012.
- [44] M. Woollacott and A. Shumway-Cook, “Attention and the control of posture and gait: a review of an emerging area of research,” *Gait and Posture*, vol. 16, no. 1, pp. 1–14, 2002.
- [45] G. Yogev, N. Giladi, C. Peretz, S. Springer, E. Simon, and J. Hausdorff, “Dual tasking, gait rhythmicity, and Parkinson’s disease: which aspects of gait are attention demanding?” *European Journal of Neuroscience*, vol. 22, no. 5, pp. 1248–1256, 2005.
- [46] T. Harada, I. Miyai, M. Suzuki, and K. Kubota, “Gait capacity affects cortical activation patterns related to speed control in the elderly,” *Experimental Brain Research*, vol. 193, no. 3, pp. 445–454, 2009.
- [47] M. Suzuki, I. Miyai, T. Ono, I. Oda, I. Konishi, T. Kochiyama, and K. Kubota, “Prefrontal and premotor cortices are involved in adapting walking and running speed on the treadmill: an optical imaging study,” *Neuroimage*, vol. 23, no. 3, pp. 1020–1026, 2004.

- [48] K. Iseki, T. Hanakawa, J. Shinozaki, M. Nankaku, and H. Fukuyama, “Neural mechanisms involved in mental imagery and observation of gait,” *Neuroimage*, vol. 41, no. 3, pp. 1021–1031, 2008.
- [49] National Institute of Mental Health, “Neuroimaging and mental illness: A window into the brain,” 2010.
- [50] M. E. Raichle, “Behind the scenes of functional brain imaging: a historical and physiological perspective,” *Proceedings of the National Academy of Sciences*, vol. 95, no. 3, pp. 765–772, 1998.
- [51] M. Deppe, E. Ringelstein, and S. Knecht, “The investigation of functional brain lateralization by transcranial Doppler sonography,” *Neuroimage*, vol. 21, no. 3, pp. 1124–1146, 2004.
- [52] M. E. Raichle and M. A. Mintun, “Brain work and brain imaging,” *Annual Review of Neuroscience*, vol. 29, pp. 449–476, 2006.
- [53] S. K. Gujar, S. Maheshwari, I. Björkman-Burtscher, and P. C. Sundgren, “Magnetic resonance spectroscopy,” *Journal of Neuro-Ophthalmology*, vol. 25, no. 3, pp. 217–226, 2005.
- [54] G. Aguirre, E. Zarahn, and M. D’esposito, “The variability of human, BOLD hemodynamic responses,” *Neuroimage*, vol. 8, no. 4, pp. 360–369, 1998.
- [55] D. Bilecen, K. Scheffler, N. Schmid, K. Tschopp, and J. Seelig, “Tonotopic organization of the human auditory cortex as detected by BOLD-fMRI,” *Hearing Research*, vol. 126, no. 1, pp. 19–27, 1998.
- [56] R. Cabeza and L. Nyberg, “Imaging cognition II: An empirical review of 275 pet and fMRI studies,” *Journal of Cognitive Neuroscience*, vol. 12, no. 1, pp. 1–47, 2000.
- [57] O. J. Arthurs and S. Boniface, “How well do we understand the neural origins of the fMRI BOLD signal?” *Trends in Neurosciences*, vol. 25, no. 1, pp. 27–31, 2002.
- [58] G. T. Herman, *Fundamentals of computerized tomography: image reconstruction from projections*. Springer Science and Business Media, 2009.
- [59] M. Koenig, E. Klotz, B. Luka, D. J. Venderink, J. F. Spittler, and L. Heuser, “Perfusion CT of the brain: diagnostic approach for early detection of ischemic stroke.” *Radiology*, vol. 209, no. 1, pp. 85–93, 1998.
- [60] M. S. Pearce, J. A. Salotti, M. P. Little, K. McHugh, C. Lee, K. P. Kim, N. L. Howe, C. M. Ronckers, P. Rajaraman, A. W. Craft *et al.*, “Radiation exposure from CT scans in childhood and subsequent risk of leukaemia and brain tumours: a retrospective cohort study,” *The Lancet*, vol. 380, no. 9840, pp. 499–505, 2012.

- [61] A. Sodickson, P. F. Baeyens, K. P. Andriole, L. M. Prevedello, R. D. Nawfel, R. Hanson, and R. Khorasani, “Recurrent CT, cumulative radiation exposure, and associated radiation-induced cancer risks from CT of adults,” *Radiology*, vol. 251, no. 1, pp. 175–184, 2009.
- [62] D. L. Bailey, D. W. Townsend, P. E. Valk, and M. N. Maisey, *Positron emission tomography*. Springer, 2005.
- [63] A. Aaslid, T. Markwalder, and H. Nornes, “Noninvasive transcranial Doppler ultrasound recording of flow velocity in basal cerebral arteries,” *Journal of Neurosurgery*, vol. 57, no. 6, pp. 769–774, 1982.
- [64] H. Kontos, “Validity of cerebral arterial blood flow calculations from velocity measurements.” *Stroke*, vol. 20, no. 1, pp. 1–3, 1989.
- [65] P. Huber and J. Handa, “Effect of contrast material, hypercapnia, hyperventilation, hypertonic glucose and papaverine on the diameter of the cerebral arteries: Angiographic determination in man.” *Investigative Radiology*, vol. 2, no. 1, pp. 17–32, 1967.
- [66] C. Giller, G. Bowman, H. Dyer, L. Mootz, and W. Krippner, “Cerebral arterial diameters during changes in blood pressure and carbon dioxide during craniotomy,” *Neurosurgery*, vol. 32, no. 5, pp. 737–742, 1993.
- [67] B. Conrad and J. Klingelhöfer, “Dynamics of regional cerebral blood flow for various visual stimuli,” *Experimental Brain Research*, vol. 77, no. 2, pp. 437–441, 1989.
- [68] S. Evers, J. Dannert, D. Rödding, G. Rötter, and E.-B. Ringelstein, “The cerebral haemodynamics of music perception a transcranial Doppler sonography study,” *Brain*, vol. 122, no. 1, pp. 75–85, 1999.
- [69] L. M. Cupini, M. Matteis, E. Troisi, M. Sabbadini, G. Bernardi, C. Caltagirone, and M. Silvestrini, “Bilateral simultaneous transcranial Doppler monitoring of flow velocity changes during visuospatial and verbal working memory tasks,” *Brain*, vol. 119, no. 4, pp. 1249–1253, 1996.
- [70] M. E. Raichle, “A brief history of human brain mapping,” *Trends in Neurosciences*, vol. 32, no. 2, pp. 118–126, 2009.
- [71] J. P. Mehta, M. D. Verber, J. A. Wieser, B. D. Schmit, and S. M. Schindler-Ivens, “A novel technique for examining human brain activity associated with pedaling using fMRI,” *Journal of Neuroscience Methods*, vol. 179, no. 2, pp. 230–239, 2009.
- [72] B. Godde and C. Voelcker-Rehage, “More automation and less cognitive control of imagined walking movements in high-versus low-fit older adults,” *Frontiers in Aging Neuroscience*, vol. 2, 2010.

- [73] H. Fukuyama, Y. Ouchi, S. Matsuzaki, Y. Nagahama, H. Yamauchi, M. Ogawa, J. Kimura, and H. Shibasaki, “Brain functional activity during gait in normal subjects: a SPECT study,” *Neuroscience Letters*, vol. 228, no. 3, pp. 183–186, 1997.
- [74] M. Higuchi, N. Okamura, K. Ishii, D. Bereczki, and H. Sasaki, “<sup>18</sup>F-FDG PET mapping of regional brain activity in runners,” *The Journal of Sports Medicine and Physical Fitness*, vol. 41, pp. 11–7, 2001.
- [75] B.-K. Min, M. J. Marzelli, and S.-S. Yoo, “Neuroimaging-based approaches in the brain–computer interface,” *Trends in Biotechnology*, vol. 28, no. 11, pp. 552–560, 2010.
- [76] M. M. Khalil, J. L. Tremoleda, T. B. Bayomy, and W. Gsell, “Molecular SPECT imaging: an overview,” *International Journal of Molecular Imaging*, vol. 2011, 2011.
- [77] E. B. Ringelstein, D. W. Droste, V. L. Babikian, D. H. Evans, D. G. Grosset, M. Kaps, H. S. Markus, D. Russell, M. Siebler *et al.*, “Consensus on microembolus detection by TCD,” *Stroke*, vol. 29, no. 3, pp. 725–729, 1998.
- [78] P. Schmidt, T. Krings, K. Willmes, F. Roessler, J. Reul, and A. Thron, “Determination of cognitive hemispheric lateralization by functional transcranial Doppler cross-validated by functional MRI,” *Stroke*, vol. 30, no. 5, pp. 939–945, 1999.
- [79] S. Duschek and R. Schandry, “Functional transcranial Doppler sonography as a tool in psychophysiological research,” *Psychophysiology*, vol. 40, no. 3, pp. 436–454, 2003.
- [80] P. Verboom, H. van Tinteren, O. S. Hoekstra, E. F. Smit, J. H. Van Den Bergh, A. J. Schreurs, R. A. Stallaert, P. C. van Velthoven, E. F. Comans, F. W. Diepenhorst *et al.*, “Cost-effectiveness of FDG-PET in staging non-small cell lung cancer: the PLUS study,” *European Journal of Nuclear Medicine and Molecular Imaging*, vol. 30, no. 11, pp. 1444–1449, 2003.
- [81] J. Fletcher, M. Clark, F. Sutton, R. Wellings, and K. Garas, “The cost of MRI: changes in costs 1989-1996.” *The British Journal of Radiology*, vol. 72, no. 857, pp. 432–437, 1999.
- [82] W. Hartje, E. Ringelstein, B. Kistingner, D. Fabianek, and K. Willmes, “Transcranial Doppler ultrasonic assessment of middle cerebral artery blood flow velocity changes during verbal and visuospatial cognitive tasks,” *Neuropsychologia*, vol. 32, no. 12, pp. 1443–1452, 1994.
- [83] D. Droste, A. Harders, and E. Rastogi, “A transcranial Doppler study of blood flow velocity in the middle cerebral arteries performed at rest and during mental activities,” *Stroke*, vol. 20, no. 8, pp. 1005–1011, 1989.
- [84] M. Bulla-Hellwig, J. Vollmer, A. Götzen, W. Skreczek, and W. Hartje, “Hemispheric asymmetry of arterial blood flow velocity changes during verbal and visuospatial tasks,” *Neuropsychologia*, vol. 34, no. 10, pp. 987–991, 1996.

- [85] R. Kelley, J. Chang, N. Scheinman, B. Levin, R. Duncan, and S. Lee, “Transcranial Doppler assessment of cerebral flow velocity during cognitive tasks,” *Stroke*, vol. 23, no. 1, pp. 9–14, 1992.
- [86] G. Vingerhoets and N. Stroobant, “Lateralization of cerebral blood flow velocity changes during cognitive task: a simultaneous bilateral transcranial Doppler study,” *Stroke*, vol. 30, no. 10, pp. 2152–2158, 1999.
- [87] L. Brass, S. Pavlakis, and D. DeVivo, “Transcranial Doppler measurements of the middle cerebral artery. Effect of hematocrit.” *Stroke*, vol. 19, no. 12, pp. 1466–1469, 1988.
- [88] J. Reid and M. Spencer, “Ultrasonic Doppler technique for imaging blood vessels,” *Science*, vol. 176, no. 4040, pp. 1235–1236, 1972.
- [89] C. Bishop, S. Powell, D. Rutt, and N. Browse, “Transcranial Doppler measurement of middle cerebral artery blood flow velocity: a validation study.” *Stroke*, vol. 17, no. 5, pp. 913–915, 1986.
- [90] F. Larsen, K. Olsen, B. Hansen, O. Paulson, and G. Knudsen, “Transcranial Doppler is valid for determination of the lower limit of cerebral blood flow autoregulation,” *Stroke*, vol. 25, no. 10, pp. 1985–1988, 1994.
- [91] H. White and B. Venkatesh, “Applications of transcranial Doppler in the ICU: a review,” *Intensive Care Medicine*, vol. 32, no. 7, pp. 981–994, 2006.
- [92] K. Lindegaard, T. Lundar, J. Wiberg, D. Sjøberg, R. Aaslid, and H. Nornes, “Variations in middle cerebral artery blood flow investigated with noninvasive transcranial blood velocity measurements,” *Stroke*, vol. 18, no. 6, pp. 1025–1030, 1987.
- [93] P. Fox and M. Raichle, “Focal physiological uncoupling of cerebral blood flow and oxidative metabolism during somatosensory stimulation in human subjects,” *Proceedings of the National Academy of Sciences of the United States of America*, vol. 83, no. 4, pp. 1140–1144, 1986.
- [94] A. Phillips, P. Ainslie, A. Krassioukov, and D. Warburton, “Regulation of cerebral blood flow after spinal cord injury,” *Journal of Neurotrauma*, vol. 30, pp. 1551–1563, 2013.
- [95] M. Globus, E. Melamed, A. Keren, D. Tzivoni, C. Granot, S. Lavy, and S. Stern, “Effect of exercise on cerebral circulation,” *Journal of Cerebral Blood Flow and Metabolism*, vol. 3, no. 3, pp. 287–290, 1983.
- [96] K. Herholz, W. Buskies, M. Rist, G. Pawlik, W. Hollmann, and W. Heiss, “Regional cerebral blood flow in man at rest and during exercise,” *Journal of Neurology*, vol. 234, no. 1, pp. 9–13, 1987.

- [97] P. Madsen, B. Sperling, T. Warming, J. Schmidt, N. Secher, G. Wildschiodtz, S. Holm, and N. Lassen, “Middle cerebral artery blood velocity and cerebral blood flow and  $O_2$  uptake during dynamic exercise,” *Journal of Applied Physiology: Respiratory, Environmental and Exercise Physiology*, vol. 74, no. 1, pp. 245–250, 1993.
- [98] L. Jorgensen, G. Perko, and N. Secher, “Regional cerebral artery mean flow velocity and blood flow during dynamic exercise in humans,” *Journal of Applied Physiology: Respiratory, Environmental and Exercise Physiology*, vol. 73, no. 5, pp. 1825–1830, 1992.
- [99] D. Delignières and K. Torre, “Fractal dynamics of human gait: a reassessment of the 1996 data of Hausdorff et al.” *Journal of Applied Physiology: Respiratory, Environmental and Exercise Physiology*, vol. 106, no. 4, pp. 1272–1279, 2009.
- [100] J. M. Hausdorff, P. L. Purdon, C. Peng, Z. Ladin, J. Y. Wei, and A. L. Goldberger, “Fractal dynamics of human gait: stability of long-range correlations in stride interval fluctuations,” *Journal of Applied Physiology: Respiratory, Environmental and Exercise Physiology*, vol. 80, no. 5, pp. 1448–1457, 1996.
- [101] J. M. Hausdorff, C. Peng, Z. Ladin, J. Y. Wei, and A. L. Goldberger, “Is walking a random walk? evidence for long-range correlations in stride interval of human gait,” *Journal of Applied Physiology: Respiratory, Environmental and Exercise Physiology*, vol. 78, no. 1, pp. 349–358, 1995.
- [102] A. Schaefer, J. S. Brach, S. Perera, and E. Sejdić, “A comparative analysis of spectral exponent estimation techniques for  $1/f^\beta$  processes with applications to the analysis of stride interval time series,” *Journal of Neuroscience Methods*, vol. 222, pp. 118–130, 2014.
- [103] D. Delignières, M. Fortes, and G. Ninot, “The fractal dynamics of self-esteem and physical self,” *Nonlinear Dynamics in Psychology and Life Sciences*, vol. 8, pp. 479–510, 2004.
- [104] R. T. Collins, R. Gross, and J. Shi, “Silhouette-based human identification from body shape and gait,” in *Proceedings of the Fifth IEEE International Conference on Automatic Face and Gesture Recognition*. Washington, DC, 21-21 May 2002, pp. 366–371.
- [105] L. Wang, T. Tan, H. Ning, and W. Hu, “Silhouette analysis-based gait recognition for human identification,” *IEEE Transactions on Pattern Analysis and Machine Intelligence*, vol. 25, no. 12, pp. 1505–1518, 2003.
- [106] D. Meyer, J. Denzler, and H. Niemann, “Model based extraction of articulated objects in image sequences for gait analysis,” in *Proceedings of the International Conference on Image Processing*, vol. 3. Santa Barbara, CA, 26-29 October 1997, pp. 78–81.
- [107] M. S. Nixon, J. N. Carter, D. Cunado, P. S. Huang, and S. Stevenage, “Automatic gait recognition,” in *Biometrics*. Springer, 1996, pp. 231–249.

- [108] H. J. Ailisto, M. Lindholm, J. Mantyjarvi, E. Vildjiounaite, and S.-M. Makela, “Identifying people from gait pattern with accelerometers,” in *Proceedings of the 8th conference on Human-computer interaction with mobile devices and services*, vol. 5779. Orlando, FL, 5 April 2005, pp. 7–14.
- [109] L. Pan, A. Chortos, G. Yu, Y. Wang, S. Isaacson, R. Allen, Y. Shi, R. Dauskardt, and Z. Bao, “An ultra-sensitive resistive pressure sensor based on hollow-sphere microstructure induced elasticity in conducting polymer film,” *Nature Communications*, vol. 5, 2014.
- [110] C. S. Sander, J. W. Knutti, and J. D. Meindl, “A monolithic capacitive pressure sensor with pulse-period output,” *IEEE Transactions on Electron Devices*, vol. 27, no. 5, pp. 927–930, 1980.
- [111] R. Aaslid, “The Doppler principle applied to measurement of blood flow velocity in cerebral arteries,” in *Transcranial Doppler Sonography*. Springer, 1986, pp. 22–38.
- [112] H. Gray, *Anatomy of the human body*. Lea Febiger, 1918.
- [113] S. Duschek and R. Schandry, “Cognitive performance and cerebral blood flow in essential hypotension,” *Psychophysiology*, vol. 41, no. 6, pp. 905–913, 2004.
- [114] W. Kuschinsky, “Coupling of function, metabolism, and blood flow in the brain,” *Neurosurgical Review*, vol. 14, no. 3, pp. 163–168, 1991.
- [115] A. Villringer and U. Dirnagl, “Coupling of brain activity and cerebral blood flow: basis of functional neuroimaging.” *Cerebrovascular and Brain Metabolism Reviews*, vol. 7, no. 3, pp. 240–276, 1994.
- [116] H. Markus and M. Boland, “Cognitive activity monitored by non-invasive measurement of cerebral blood flow velocity and its application to the investigation of cerebral dominance,” *Cortex*, vol. 28, no. 4, pp. 575–581, 1992.
- [117] R. W. Gill, “Pulsed Doppler with B-mode imaging for quantitative blood flow measurement,” *Ultrasound in Medicine and Biology*, vol. 5, no. 3, pp. 223–235, 1979.
- [118] H. Azhari, *Basics of biomedical ultrasound for engineers*. John Wiley Sons, 2010.
- [119] D. Benitez, P. Gaydecki, A. Zaidi, and A. Fitzpatrick, “The use of the Hilbert transform in ECG signal analysis,” *Computers in Biology and Medicine*, vol. 31, no. 5, pp. 399–406, 2001.
- [120] P. Schneider, M. Rossman, E. Bernstein, S. Torem, E. Ringelstein, and S. Otis, “Effect of internal carotid artery occlusion on intracranial hemodynamics. Transcranial Doppler evaluation and clinical correlation,” *Stroke*, vol. 19, no. 5, pp. 589–593, 1988.

- [121] A. Alexandrov, M. Sloan, L. Wong, C. Douville, A. Razumovsky, W. Koroshetz, M. Kaps, and C. Tegeler, “Practice standards for transcranial Doppler ultrasound: part I – test performance,” *Journal of Neuroimaging*, vol. 17, no. 1, pp. 11–18, 2007.
- [122] E. Sejdić, D. Kalika, and N. Czarnek, “An analysis of resting-state functional transcranial Doppler recordings from middle cerebral arteries,” *PLoS One*, vol. 8, no. 2, 2013.
- [123] I. Simonsen, A. Hansen, and O. M. Nes, “Determination of the Hurst exponent by use of wavelet transforms,” *Physical Review E*, vol. 58, pp. 2779–2787, Sep 1998.
- [124] A. Papoulis, *Probability, Random Variables, and Stochastic Processes*. WCB/McGraw-Hill, 1991.
- [125] G. Tiao and G. Box, “Modeling multiple time series with applications,” *Journal of The American Statistical Association*, vol. 76, no. 376, pp. 802–816, 1981.
- [126] S. Ahmed, M. Shahjahan, and K. Murase, “A Lempel-Ziv Complexity-based neural network pruning algorithm,” *International Journal of Neural Systems*, vol. 21, no. 5, pp. 427–441, 2011.
- [127] S. Pincus, I. Gladstone, and R. Ehrenkranz, “A regularity statistic fore medical data analysis,” *Journal of Clinical Monitoring*, vol. 7, no. 4, pp. 335–345, 1991.
- [128] J. Hu, J. Gao, and J. Principe, “Analysis of biomedical signals by the Lempel-Ziv Complexity: the effect of finite data size,” *IEEE Transactions on Biomedical Engineering*, vol. 53, no. 12, pp. 2606–2609, 2006.
- [129] A. Lempel and J. Ziv, “On the complexity of finite sequences,” *IEEE Transactions on Information Theory*, vol. 22, no. 1, pp. 75–81, 1976.
- [130] A. Porta, S. Guzzetti, N. Montano, R. Furlan, M. Pagani, and V. Somers, “Entropy, entropy rate, and pattern classification as tools to typify complexity in short heart period variability series,” *IEEE Transactions on Information Theory*, vol. 48, no. 11, pp. 1282–1291, 2011.
- [131] A. Porta, S. Guzzetti, N. Montano, M. Pagani, V. Somers, A. Malliani, G. Baselli, and S. Cerutti, “Information domain analysis of cardiovascular variability signals: evaluation of regularity, synchronisation and co-ordination,” *Medical and Biological Engineering and Computing*, vol. 38, no. 2, pp. 180–188, 2000.
- [132] A. Porta, G. Baselli, D. Liberati, N. Montano, C. Cogliati, T. Gneccchi-Ruscone, A. Malliani, and S. Cerutti, “Measuring regularity by means of a corrected conditional entropy in sympathetic outflow,” *Biological Cybernetics*, vol. 78, no. 1, pp. 71–78, 1998.
- [133] L. Vergara, J. Gosalbéz, J. Fuente, R. Miralles, and I. Bosch, “Measurement of cement porosity by centroid frequency profiles of ultrasonic grain noise,” *Biomedical Engineering Online*, vol. 84, no. 12, pp. 2315–2324, 2004.

- [134] J. Allen, “Short-term spectral analysis, and modification by discrete fourier transform,” *IEEE Transactions on Audio and Electroacoustics*, vol. 25, no. 3, pp. 235–238, 1977.
- [135] L. Cohen, “Time-frequency distributions-a review,” *Proceedings of the IEEE*, vol. 77, no. 7, pp. 941–981, 1989.
- [136] O. Rioul and M. Vetterli, “Wavelets and signal processing,” *IEEE Signal Processing Magazine*, vol. 8, pp. 14–38, 1991.
- [137] R. X. Gao and R. Yan, *Wavelets: Theory and applications for manufacturing*. Springer Science Business Media, 2010.
- [138] I. Daubechies *et al.*, *Ten lectures on wavelets*. Society for Industrial and Applied Mathematics, 1992, vol. 61.
- [139] S. G. Mallat, “A theory for multiresolution signal decomposition: the wavelet representation,” *IEEE Transactions on Pattern Analysis and Machine Intelligence*, vol. 11, no. 7, pp. 674–693, 1989.
- [140] C. S. Burrus, R. A. Gopinath, and H. Guo, *Introduction to wavelets and wavelet transforms: A primer*. Prentice Hall, 1998, vol. 998.
- [141] M. Hilton, “Wavelet and wavelet packet compression of electrocardiograms,” *IEEE Transactions on Biomedical Engineering*, vol. 44, no. 5, pp. 394–402, 1997.
- [142] O. Rosso, S. Blanco, J. Yordanova, V. Kolev, A. Figliola, M. Schürmann, and E. Basar, “Wavelet entropy: a new tool for analysis of short duration brain electrical signals,” *Journal of Neuroscience Methods*, vol. 105, no. 1, pp. 65–75, 2001.
- [143] Y. Benjamini and Y. Hochberg, “Controlling the false discovery rate: a practical and powerful approach to multiple testing,” *Journal of the Royal Statistical Society. Series B (Methodological)*, pp. 289–300, 1995.